ACS Sustainable Chemistry & Engineering

pubs.acs.org/journal/ascecg

Research Article

Molecular Mechanism and Electrostatic Effect Enabling Symmetric All-Quinone Aqueous Redox Flow Batteries

José Eduardo dos Santos Clarindo, Rafael Neri Prystaj Colombo, Graziela Cristina Sedenho, Luana Cristina Italiano Faria, Thiago Bertaglia, Filipe Camargo Dalmatti Alves Lima, Roberto da Silva Gomes, Michael J. Aziz, and Frank Nelson Crespilho*

Cite This: https://doi.org/10.1021/acssuschemeng.3c08218

ABSTRACT: Symmetric all-quinone aqueous redox flow batteries (SQA-RFBs), in which the same quinone derivative is used as the electroactive compound in the negative and positive electrolytes, thereby obviating the need for a species-selective membrane, have been pursued as a potentially cost-effective and sustainable technology for stationary-electrical energy storage. Molecular decomposition during redox activity has frustrated all symmetric organic aqueous RFB development attempts. We used in situ/operando spectroelectrochemistry and density functional theory calculations to demonstrate that during the redox reaction of alizarin red S (ARS), a promising quinone for SQA-RFBs, intramolecular electronic oscillations form positively charged intermediates. Electrodes functionalized with net negative charge stabilize these intermediates via a hybrid adsorptive−diffusive electrochemical reaction mechanism, thereby enabling the cycling of the SQA-RFB. To understand the mechanism, spectroelectrochemical studies were performed on a series of electrodes with and without this functionalization. We report the performance of the first membraneless SQA-RFB prototype, containing ARS in the electrolyte storage reservoirs and instrumented with a reference electrode to evaluate the evolution of the half-cell potentials.

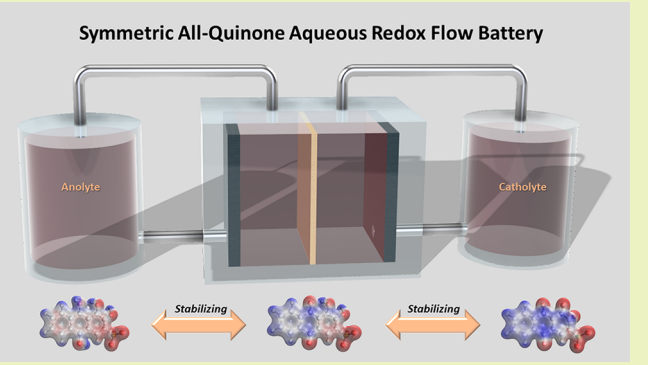

KEYWORDS: *redox flow battery, quinone, symmetric battery, alizarin red S, carbon electrode*

INTRODUCTION

In recent years, renewable energy sources have emerged as a highlighted trend for application in the field of energy conversion in the environmental context of decarbonization of energy industries with future near-net-zero emission targets.[1,2] Most renewable energy, however, suffers from intermittency due to the dependence on wind or solar cycles; therefore, advances in the development of electrical storage units are in demand.[3−6] These storage units are desirable to supply grid leveling, complementing demand−response applications and efforts to continental scale transmission, and therefore of interest for eco-friendly and sustainable energy generation matrices.

Among possible electrical storage units are redox flow batteries (RFBs), which are electrochemical devices in which electrical energy is stored and is converted to/from the chemical energy of two chemical components stored in external reservoirs and flown to the conversion cell during cycling.[7,8] The most heavily commercialized RFB technology is based on storing energy in four distinct charge states of vanadium in a symmetric inorganic vanadium-bearing acidic electrolyte, especially after the 1980s.[9] After decades of vanadium-based RFB development, organic aqueous RFBs emerged in 2014, in which energy is stored in potentially inexpensive redox-active organic molecules.[10−12] The limited availability and high cost of vanadium, as well as safety concerns, have limited the widespread deployment of vanadium-based RFBs.[13,14] Recent works have expanded the discussions concerning RFB attributes, bottlenecks, and benchmarking, enabling advances in the field.[15]

Quinones show great promise for use in RFBs due to several factors, such as (i) they are entirely composed of earth-abundant elements, such as carbon, oxygen, and hydrogen; (ii) their molecular properties can be tuned via molecular engineering; and (iii) they have been demonstrated to act effectively in negative electrolytes, with satisfactory stability, solubility, and performance.[16] Because quinones constitute a class of metal-free molecules that comprise earth-abundant

Received: December 14, 2023
Revised: June 28, 2024
Accepted: July 1, 2024

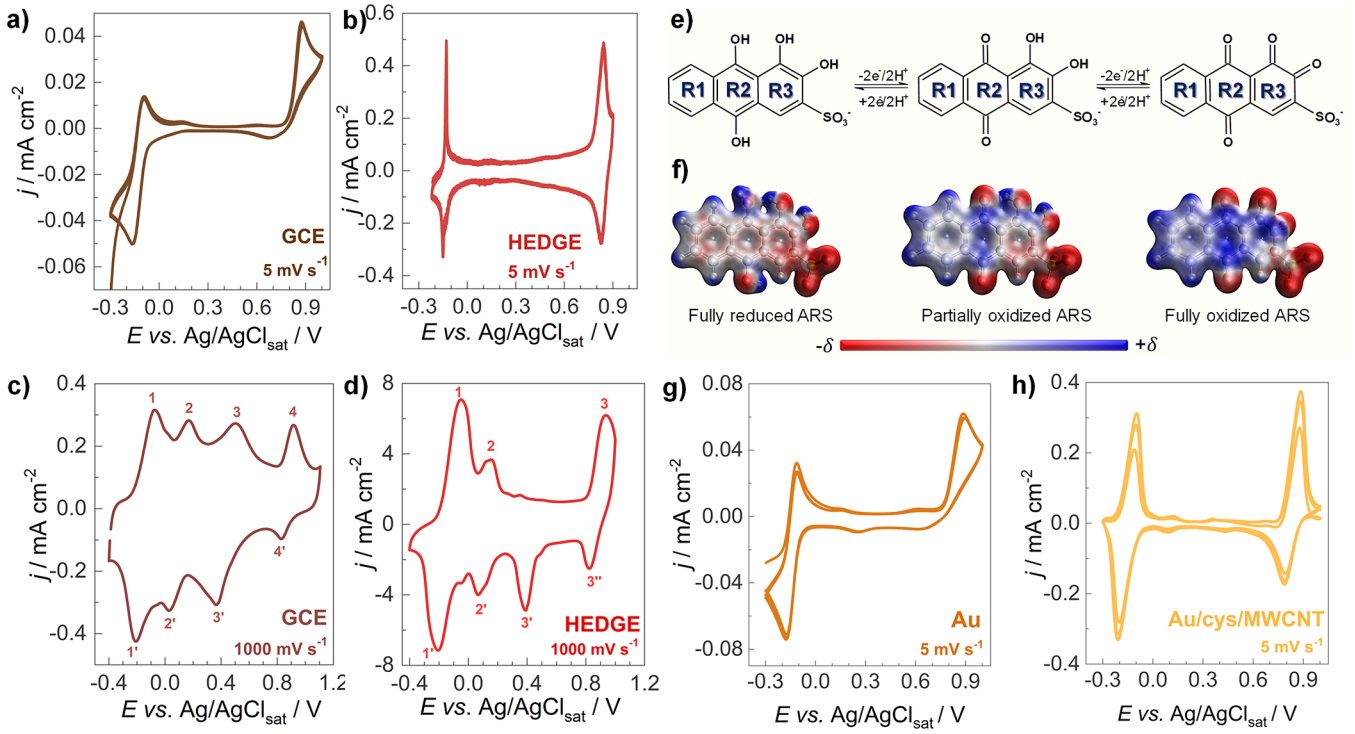

Figure 1. CVs of (a) bare GCE disc and (b) HEDGEs, in 1.0 mmol L^{-1} ARS in 1.0 mol L^{-1} H_2SO_4 solution (5 mV s^{-1}), highlighting the reversibility of the low-potential redox process and the strong dependence of the high-potential process on the electrode matrix. High-speed CVs (1000 mV s^{-1}) of adsorbed ARS onto (c) GCE and (d) HEDGE, emphasizing additional intermediate redox processes seen only at high scan rates. (e) Schematic of the redox interconversions of ARS from the fully reduced to the fully oxidized state. (f) MEPs of the three redox states of ARS obtained through DFT calculations, colored to exhibit the charge concentration and charge localization differences. CVs of (g) bare Au electrode and (h) Au/cys/MWCNT electrode in 1.0 mmol L^{-1} ARS in 1.0 mol L^{-1} H_2SO_4 solution (5 mV s^{-1}), indicating the electrostatic stabilization effect of the negative charges (later shown being due to −COOH groups) onto the positive rings of the fully oxidized ARS, leading to the reversible redox process and sharp peaks (electrostatic affinity).

elements, they provide potentially low-cost RFB energy storage solutions.[7,10,16,17] More than 140,000 quinone pairs have been computationally analyzed to identify ideal redox components, suggesting that many quinones with low reduction potential are stable.[18] Additionally, molecular engineering strategies show the possibility of fine-tuning the redox potential and solubility through hydrogen interactions and substituent modifications.[19] In contrast, few high redox potential quinones were predicted as stable against known decomposition mechanisms. To date, no high-performance quinone-based positive electrolytes have been demonstrated experimentally.

A symmetric all-quinone aqueous redox flow battery has been envisioned, in which the same quinone derivative is used in both negative and positive electrolytes; however, it has never been demonstrated. A symmetric configuration, with identical composition of the two electrolytes in the discharged state, obviates the need for a permselective membrane, thereby shedding its material cost and polarization overvoltage. Residual crossover of species in their charged states becomes merely an engineering problem of energy efficiency rather than a contamination problem requiring chemical separation and compromising long-term operational capability.[4] Several works have discussed the structural and strategic details to obtain bipolar redox-active molecules for a nonaqueous environment.[20−23] However, the decomposition of surface-unstable quinone molecules to redox-inactive products via irreversible side reactions on the electrode surface during the redox cycling becomes a significant challenge in obtaining a SQA-RFB.[18]

Recently, a symmetric anthraquinone solid battery with alizarin red sulfonated (ARS) molecules (Figure 1) has been demonstrated, in which ARS was incorporated into a carbonaceous matrix immobilized on carbon-based electrodes.[24] ARS is considered an unstable redox molecule in solution because the signal observed for the high-potential redox couple exhibits a prominent oxidation peak but little or no corresponding reduction peak. However, when ARS is adsorbed onto the electrode surface, this abnormal behavior is suppressed. It was hypothesized that ARS undergoes two separate one-electron processes during oxidation and that, in solution, the intermediate radical may diffuse away and undergo subsequent degradation before experiencing further oxidation to afford the stable tetraone form.[18,24,25] Thus, the formation of some hitherto unidentified radical intermediates may be preventing reversible oxidation and reduction of the high-potential couple.

Although many quinone derivatives can undergo thermodynamically reversible proton-coupled electron-transfer reactions in solution, we have recently shown that the electrochemical reversibility of the high-potential redox pair of some of these compounds is affected by their molecular structure as well as by the properties of the electrode surface.[26] Combining experimental observations, molecular dynamics simulations, and quantum mechanics calculations, we proposed that defects with oxygen-containing functional groups, such as C−O and C═O, on carbon-based electrodes afford greater stabilization of unstable quinone/semiquinone radical intermediates on the electrode's surface.[26] This result appears to be counterintuitive

https://doi.org/10.1021/acssuschemeng.3c08218
ACS Sustainable Chem. Eng. XXXX, XXX, XXX−XXX

because it is expected that quinones with negative net charge would be repelled by negatively charged electrode surfaces with oxygenated groups. As we show here, electrostatic potential topology indicates a charge fluctuation effect (charge polarization instability) on quinone derivative molecules under electrochemical bias, which makes the aromatic rings remain positively charged. Building upon this insight, we propose that negatively functionalized electrodes can be designed to correctly stabilize these intermediates, allowing the operation of an ARS-based SQA-RFB. Here, we show how this can be accomplished, using appropriate chemical treatment processes for carbonaceous electrodes. We provide a detailed understanding of the molecular structures and processes involved in ARS redox processes. Finally, we demonstrate the first membraneless SQA-RFB prototype, improving costs from conventional selective membranes,[27,28] and evaluate the evolution of the half-cell potentials utilizing a reference electrode.

Symmetric Quinone: The Origin of Charge Polarization Instability. ARS contains two quinone functional groups; hence, its cyclic voltammogram (CV) exhibits two redox events, the first one at lower potentials (ca. −0.14 V), assigned to the $C_{9,10}$ ARS group, and the second one, at higher potentials (ca. + 0.85 V) assigned to the $C_{1,2}$ ARS group. The electrochemical reversibility of the redox event at high redox potential is drastically affected by the structural and chemical features of the carbon electrodes.[26] To investigate the reasons for this, we selected three different carbon electrodes to explore the effects of the electrode material on the electron-transfer kinetics and thermodynamics of ARS. A glassy carbon electrode (GCE) and a high-edge-density graphite electrode (HEDGE) are carbon-based materials with distinct features, with the HEDGE having a higher density of structural defects and oxygen functional groups than the GCE.[26] As promising electrodes for a RFB, we also studied HPCCE-5H, a flexible and versatile carbon cloth with improved mechanical stability and electrochemical performance compared to conventional carbon paper electrodes.[29,30] All potentials described here are reported against a $Ag/AgCl/Cl^-_{sat}$ reference electrode.

The CV of purified ARS on the GCE (Figure 1a, purification details shown in Figure S1, CVs of all electrodes in 1.0 mol L^{-1} H_2SO_4 without ARS are shown in Figure S2) exhibits an oxidation peak at −0.094 V and a major reduction peak at −0.165 V, with a peak-to-peak separation (ΔE_p) of 71 mV, indicating quasi-reversible redox reactions along with mass transfer. At high potentials, a prominent oxidation peak is observed at 0.872 V, but only a barely recognizable reduction peak is observed at 0.684 V, suggesting that the 1,2-quinone group undergoes an irreversible electrochemical reaction. In contrast, two well-defined reversible redox processes are observed on the HEDGE (Figure 1b), with low-potential peaks at −0.130 and −0.150 V (i.e., ΔE_p = 20 mV) and high-potential peaks at 0.842 and 0.825 V (ΔE_p = 17 mV). This suggests improved stability of the oxidized molecule while adsorbed to this electrode material. Additionally, the narrow peak shape on the HEDGE suggests a strongly attractive interaction of the adsorbed molecule to this electrode surface.[31] These differences are related to the presence of edge-like defects and the high amounts of C═O and C−O groups on the HEDGE, as previously discussed.[26]

To observe the electron-transfer rates of the ARS, CVs were recorded with a GCE and a HEDGE at high scan rates (Figure 1c,d). We can see at least two additional redox processes at high scan rates, at half-wave potentials ($E_{1/2}$) of 0.087 and 0.430 V, intermediate between those of the two common redox processes, which can be attributed to the formation of radicals during the oxidation and reduction processes, as reported in the literature on anthraquinone-based redox-active molecules.[17,32−34] Based on the electrochemical and spectroscopic data presented below, a mechanism evidencing the formed radicals will be offered.

To provide further insights into the stabilization of adsorbed ARS granting improved reversibility of the reactions (Figure 1e), we performed computational studies on the electrostatic potential topology, which is a powerful tool to probe molecular interaction and reactivity,[35] by generating surface potential maps (MEPs) for the three redox states. The results (Figure 1f) show the evident negatively charged sites (red) concentrated at the sulfonic acid and oxygen atoms of the hydroxyl groups, which become even more negatively charged as hydroxyls are oxidized to carbonyls. Interestingly, an electrostatic trend is also observed in the aromatic rings. In the reduced state, the three rings are slightly negatively charged, and when $C_{9,10}$−OH is converted to C═O, the first ring (R1) becomes slightly positive (blue colored), and the second ring (R2) becomes more positively charged, which matches the expected dipole induced by the carbonyls attached to this ring. The third ring (R3) retains a negative charge, in an opposite polarity from the first ring. This indicates that changes in electrostatic interactions during the redox processes could be the factor governing the stability of molecules on a charged electrode. Additionally, the importance of the presence of oxidized functional groups to drive a higher affinity of the oxidized ARS, allowing the occurrence of the reverse reduction process, is highlighted.

To further investigate this behavior and test the hypothesis of the electrostatic-induced stabilization effect, we modified a gold electrode, which cannot stabilize the oxidized form by itself, as shown in the CV (Figure 1g). The gold electrode modified with carboxylated multiwalled carbon nanotubes (MWCNTs) and cysteamine provides (i) diffuse-positive charges to stabilize the negatively charged rings in the reduced state, (ii) also negatively charged carboxylates for the oxidized ARS via $-COO^-$ groups in the MWCNTs, and (iii) MWCNTs have been shown to provide adsorption-based stabilization of anthracenes via strong and long-displacement-range aromatic π-stacking interactions,[36,37] which is once again desirable. The CV results (Figure 1h) indicate that an electrostatic stabilization, later shown as being due to carboxylates, plays a major role in the reversibility of the high-oxidation-state form of ARS, confirming our hypothesis. Furthermore, differential pulse voltammetry (DPV) indicates that the high density of negative functional groups in the electrode material allows the visualization of additional redox peaks at 0.113 and 0.425 V (Figure S3), which is provisionally understood to be the semiquinone radical electron-transfer process and was only seen during fast-scan voltammetry (Figure 1c,d), at similar potentials; the DPV suggests that the main peaks correspond to a one-electron process, which reinforces the idea of radical stabilization requirements for improved redox reversibility of the quinones. The appearance of these redox processes highlights the importance of a tailored interaction between the electrode and the redox-active organic molecule.

Because the manipulation of HEDGEs for a RFB suffers from the lack of mechanical flexibility and brittleness of the

https://doi.org/10.1021/acssuschemeng.3c08218
ACS Sustainable Chem. Eng. XXXX, XXX, XXX−XXX

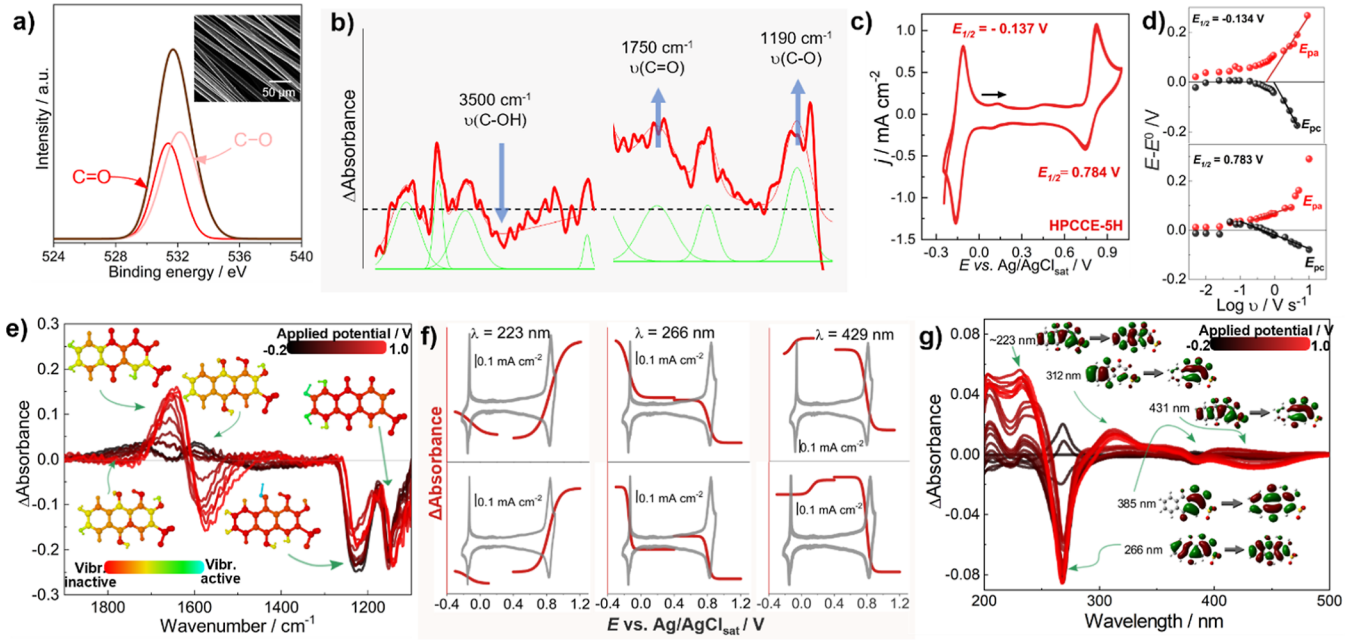

Figure 2. a) Oxygen 1s XPS spectrum of HPCCE-5H, emphasizing the presence of surface-oxidized groups as organic C−O and C═O. (b) HPCCE-5H FTIR spectra with deconvoluted bands of the main carbon−oxygen functional groups, emphasizing the presence of oxidized groups as carboxylic acids, with a minor hydroxyl content. (c) CV of HPCCE-5H fibers in the presence of ARS (1.0 mmol L^{-1} ARS solution in 1.0 mol L^{-1} H_2SO_4), scan rate of 5 mV s^{-1}. (d) Peak potentials as functions of the log of scan rate for the low- and high-potential redox pairs, for the heterogeneous electron-transfer rate constant calculation through the Laviron model. (e) In situ ARS FTIR spectra collected from −0.2 to +1.0 V, employing a polycrystalline gold electrode in acidic medium (0.1 mmol L^{-1} ARS solution in 1.0 mol L^{-1} H_2SO_4), with a black-red color gradient indicating the redox potential from most negative (black) to most positive (red) potentials; additionally, a rainbow color gradient indicates most vibrational active (blue) and inactive (red) portions of the molecules corresponding to the vibrational modes at each band, as calculated through DFT; larger image in the Supporting Information. (f) Nernst-fitted functions for main excited state (223, 266, and 429 nm) transitions in the in situ electrochemically coupled electronic spectroscopy, depicting high dependence of the transitions to the redox state. Here, the electronic transitions are monitored concomitantly/real time to the potential sweep. (g) In situ UV−vis spectroscopy of ARS (1.0 mmol L^{-1} ARS solution in 1.0 mol L^{-1} H_2SO_4), collected at increasing potentials from −0.2 to +1.2 V, with main molecular orbital transitions represented as calculated through TD-DFT (see the Supporting Information for additional details) for each peak; an enlarged and more detailed version of 2 g is shown in the Supporting Information.

electrode, we employed a flexible carbon-fiber-based electrode, viz., HPCCE-5H, after a chemical treatment, discussed in detail in the Supporting Information file (Figure S4), to install carbonyl groups. Its X-ray photoelectron spectroscopy (XPS) analysis revealed the presence of both C−O and C═O at the surface (Figure 2a; XPS of pristine fibers in Figure S5, lacking significant C−O content). The Fourier transform infrared (FTIR) analysis of the treated carbon fibers (Figure 2b) also shows the presence of oxygenated groups, as can be seen from the modes of ν_{C-OH} at 3500 cm^{-1} which are decreased mainly due to the formation of carboxylic acids, indicated by the modes ν_{C-O} at 1750 cm^{-1} and ν_{C-O} at 1190 cm^{-1}.

Oxygenated functional groups are introduced on the surfaces of carbon cloth by chemical treatment, corroborating the fact that this feature plays an important role in the ARS electron-transfer kinetics.[29] We infer that these functional groups can be crucial contributors to interactions with the ARS functional groups and the aromatic rings because they enable charge balance for enhanced adsorption stability. Reversible electrochemical redox behavior of ARS is also observed on the treated HPCCE-5H fibers (Figure 2c), with two well-defined redox couples at lower ($E_{1/2}$ = −0.137 V) and higher potentials ($E_{1/2}$ = −0.785 V), suggesting a quasi-reversible electrochemical reaction involving both quinone groups, with a mass-transfer contribution.

In order to show that the redox processes are associated with a stabilized surface instead of diffusional events, we performed CV scans at 1 and 0.01 V s^{-1} using a 1000× dilute (10 μmol L^{-1}) ARS solution, Figure S6, showing that without favorable mass-transport conditions, the low- and high-potential pairs are only seen at high scan rates, which favors surface-associated redox processes instead of the diffusional ones. The square wave voltammogram at the micromolar regime shows the oxidation and reduction of the low- and high-redox pairs at both the forward and the backward waves, in agreement with Figure S3. This highlights that efficient reversibility is associated with surface-driven redox events.

The oxidation and reduction heterogeneous rate constants are prominently higher on electrodes containing greater amounts of structural defects and oxygenated functional groups, such as HEDGE and HPCCE-5H (Figure 2d and Table S1) than on GCE (Figures S7 and S8 and Table S1), as indicated by the experimentally obtained heterogeneous rate constant through the Laviron method (i.e., $E - E^0$ vs log ν, see the calculation in the Supporting Information, Section S4). In our measurements, ARS adsorbed onto HPCCE-5H presented heterogeneous rate constants of $k_{ox,low}$ = 21.22 ± 9.51 s^{-1}, $k_{red,low}$ = 16.62 ± 9.37 s^{-1} and $k_{ox,high}$ = 42.66 ± 11.43 s^{-1}, $k_{red,high}$ = 14.23 ± 6.91 s^{-1} for the low- and high-potential pairs, respectively, which are up to 20-fold higher than those parameters obtained with a GCE. For reference, CV signatures

https://doi.org/10.1021/acssuschemeng.3c08218
ACS Sustainable Chem. Eng. XXXX, XXX, XXX−XXX

of GCE, HEDGE, Au, and HPCCE-5H in N_2-saturated H_2SO_4 without ARS are shown in Figures S9 and S10. It is worth emphasizing the importance of the chemical treatment of the carbon fibers to increase the oxygen content, as shown by XPS spectroscopy data, and to improve the pristine HPCCE-5H's poor surface capability to stabilize oxidized ARS (evidenced in Figure S11).

Engineering Electrodes for Intermediate Stabilization. The in situ FTIR spectroelectrochemistry provides pivotal information concerning molecular groups' fingerprints at distinct electrochemical potentials,[38,39] using HPCCE-5H as the electrode material in a 1.0 mmol L^{-1} ARS solution in 1.0 mol L^{-1} H_2SO_4. To facilitate the understanding, we split the analysis into two parts: (i) functional groups and (ii) aromatic backbone modes. The analysis is discussed with attributions based on density functional theory (DFT) calculations; additional details are present in the Supporting Information and in the FTIR calculated spectra in Figure S12.

When the potential is swept toward more positive values (i.e., increasingly oxidizing), Figure 2e indicates that C═C stretching modes of the anthraquinone moiety coupled to the $C_{1,2,9,10}$−OH bending modes decrease in two sequential processes: one at less positive potentials with a smaller decrease in absorbance (ca. 1590 cm^{-1}), which indicated the oxidation of the reduced state to an intermediate state with the conversion of $C_{9,10}$−OH to $C_{9,10}$═O, preserving the hydroxyl groups at $C_{1,2}$. The second process at higher potentials induces a complete decrease in absorbance (a negative band) due to the formation of carbonyl groups at $C_{1,2}$. This process is strictly linked to the positive band at 1670 cm^{-1}, indicating inverse behavior, with a smaller increase at the same lower potentials of the first process due to the formation of $C_{9,10}$ carbonyl groups and the second process with higher absorbance when the ARS is fully oxidized, and 1,2-C hydroxyl groups are also converted to carbonyl groups. Through DFT computational calculations, distinct portions of the molecules were shown to be vibrationally active at each vibrational mode and represented by gradient coloring (Figures 2g and S12). Using this approach, we can incorporate vibrational activity information into each molecular state, enabling the visualization of localized displacements that correlate with the electrochemistry and electronic spectroscopy; this will be presented in the next section.

Additionally, as shown in Figure 2e, the reduced form of the aromatic molecule has more active stretching modes in the first and second rings, ca. 1600 cm^{-1}. The absorbance decreases in the oxidized form, while a new backbone vibrational coupled mode appears at ca. 1670 cm^{-1}, with an intense vibrational activity of the two aforementioned rings coupled to a new stretching mode at R2 and R3. Here, again, the bands corresponding to the intermediate form of the ARS lie between the bands of the fully reduced and oxidized forms of the redox molecule.

These data indicate that the redox two-step sequential conversion of hydroxyls to carbonyls occurs and that critical changes to the aromatic rings could play a role in the molecular stability.

After the second redox process, when $C_{1,2}$−OH groups are converted to C═O, the positive potentials at R1 and R2 are intensified, while R3 also becomes significantly positive, especially close to $C_{1,2}$. This once again corroborates with the FTIR vibrational data of the backbone and suggests electrostatic requirements to stabilize the adsorbed positively charged oxidized molecule, which is an effect that has been poorly explored in the literature thus far. This could, naturally, mean that negatively charged functional groups on the electrode's surface, like carboxylates, interact with the positive aromatic rings and prevent desorption, leading to a reversible process, as in HEDGE (Figure 1b) and confirmed in Au/cys/MWCNT (Figure 1f). Naturally, the lack of reversibility when an electrode cannot stabilize the oxidized state is also observed in the in situ vibrational studies, as shown for gold electrodes in Figures S13 and S14, in which the main bands of the fully oxidized form are maintained even during reduction. For reference, the solid ARS FTIR spectrum is shown in Figure S15, and the attributions are listed in Table S2.

The study of redox processes can also be complemented by in situ electronic spectroscopy (Figure 2f,g, setup shown in Figure S16, see enlarged UV−vis in Figure S17) and computational modeling probing the molecular orbital transitions via time-domain DFT (TD-DFT) calculations (Figure S18); here, H and L correspond to HOMO and LUMO, respectively. The bands at 266 nm (H − 1 → L + 1) and 385 nm (H → L) in the reduced state disappear after oxidation at ca. −0.10 V (negative peak equals absorbance signal loss), and new bands appear at 680 nm (H → L), 431 nm (H − 2 → L), 312 nm (H − 4 → L), and 223 nm (H − 2 → L + 2). The molecular orbitals clearly depict a higher degree of π-bonds and symmetrical character in the reduced and intermediate states, matching the higher content of π electrons from the rings without the electron-withdrawing effect from the carbonyls formed after the oxidation. At the same time, the electronic spectroscopy of the fully oxidized form of the molecule contains an interesting amount of σ character, predominantly localized in the third ring (see H, H − 2-to-L transitions, Figure S18), in conformity to FTIR and DFT data. The presence of this σ character in the molecular orbitals probably plays a role in the oxidized molecule's sensitivity to degradation, which was reported elsewhere in cases where the oxidized form is not stabilized via electrostatic interactions, as via 1,4-addition through a nucleophilic attack, dimerization, and even oligomerization in other quinones.[18,25,40] The molecular orbitals (MOs) of the intermediate ARS form are present as shifted bands, such as the π−π^* transition bands at 230 nm (H − 2 → L + 1) and 400 nm (H → L).

In situ electronic spectroscopy coupled to the electrochemical setup indicates that the H − 2 → L + 2 transition with σ content only appears after ca. 0.75 V (Figure 2g), it is therefore exclusive for the fully oxidized form. The H and H − 2 orbitals depict extensive σ character at the third ring and at the second to a lesser extent, showing how the oxidized form of the high-potential pair is more unstable due to the charge concentration and the electron pulling from the two new carbonyls formed, which is consistent with the mechanisms and instabilities described in the literature. The same is observed at 430 nm, where the first oxidation produces an increase in the intensity of the π−π^* band of the intermediate form, with MOs localized primarily at the second and third aromatic rings, and the high-potential oxidation process reduces the intensity of this transition concerted to an induced σ content.

The same logic can be employed in the reverse potential sweep direction, i.e., from more positive to negative electrode potentials, to investigate the reduction processes. However, because gold cannot stabilize the oxidized form, it is expected that the FTIR and UV−vis should not be simply the reverse of

https://doi.org/10.1021/acssuschemeng.3c08218
ACS Sustainable Chem. Eng. XXXX, XXX, XXX−XXX

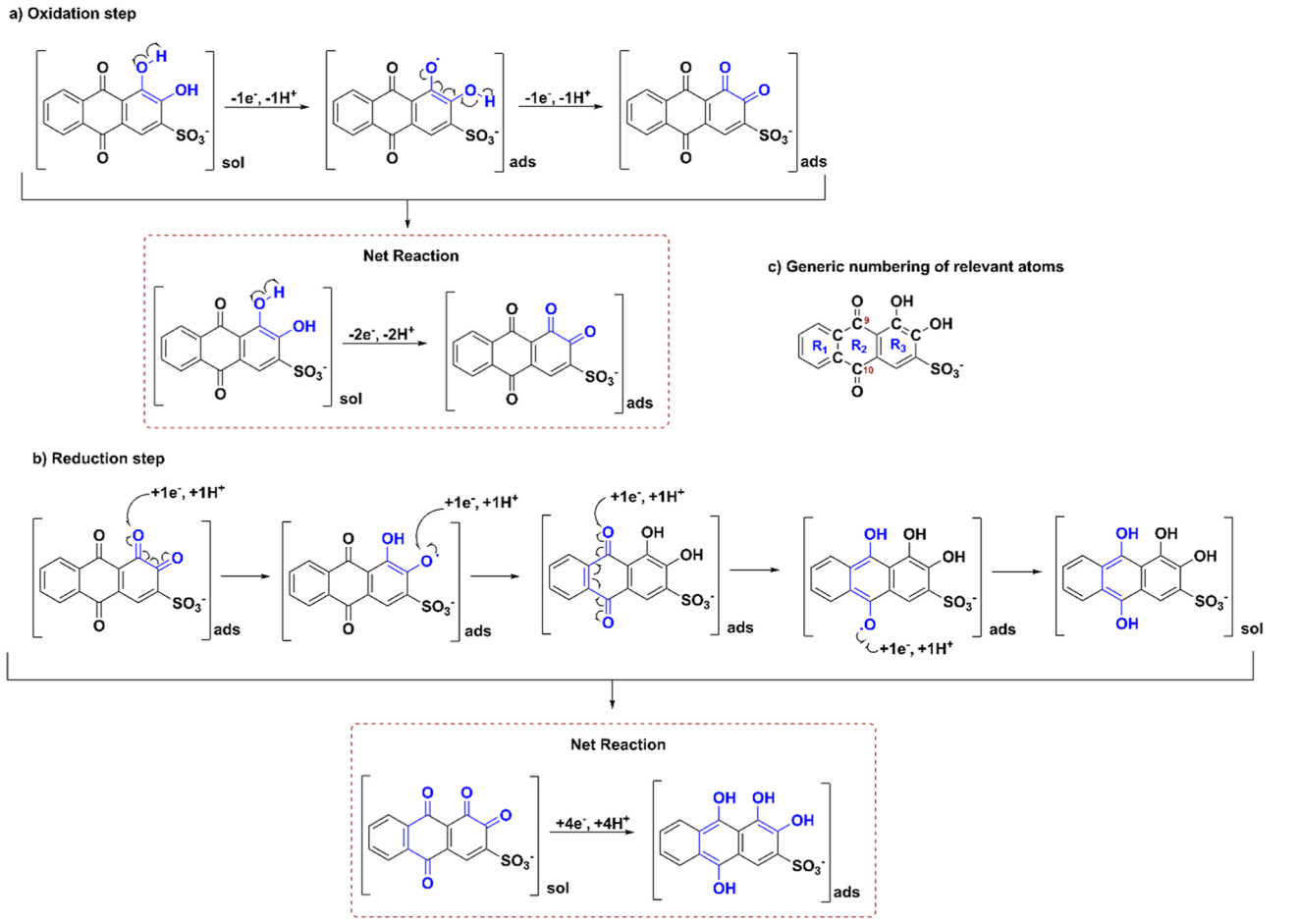

Figure 3. Proposed mechanism for the (a) sequential two coupled $-1e^-/-1H^+$ oxidation of ARS, from the intermediate to the fully oxidized form; (b) four sequential coupled $+1e^-/+1H^+$ redox processes to form the fully reduced species; (c) generic numbering of relevant atoms (in red, following anthracene traditional numbering) and cyclic rings (in blue) used herein. Highlighted parts of the structure in blue to emphasize molecular transformations. Abbreviations "sol" and "ads" stand for species in solution and species adsorbed onto the electrode surface, respectively.

those previously shown. The redox irreversibility at gold can be observed by in situ electronic spectroscopy, in which the potential sweep starting at high potentials toward the negative direction induces an increase in the $\pi-\pi^*$ transition at 266 nm, which is characteristic of the reduced form of ARS; however, the intensity of the 218 nm band (characteristic of the σ-containing MO of the oxidized form) decreases only slightly, suggesting that a major fraction of the oxidized ARS cannot be electrochemically reduced at the surface.

A similar electronic spectroscopy study was performed employing the flexible fibers HPCCE-5H (Figures S19 and S20), with the same attribution of the bands, as shown in Table S3. In this case, the reversibility of the high-potential redox process is due to the stabilization of the electrostatic charge as the third ring interacts with the oxygen content in the fibers, thus preserving the spectroscopic signature in the reverse scan (i.e., from the oxidized to the reduced states). This is presented as a broadening in the UV region, and overall hypsochromic shift, once again corroborating the loss of conjugation by the fraction of nonreduced molecules.

General ARS Redox Mechanistic Considerations. The association of in situ vibrational and electronic spectroscopy, coupled with electrochemical control and DFT calculations, allows us to propose the following redox mechanism.

We propose that the net redox mechanism involves two steps. The oxidation of the intermediate form comprises the oxidation of the hydroxyl group at C_1 (Figure 3a), involving the loss of $1e^-/1H^+$ via a radical electron-transfer step favored by the electrode surface. The stability of the radical, by resonance, favors the immediate and subsequential loss of another $1e^-/1H^+$ at the hydroxyl group at C_2 to form the completely oxidized form, in a net reaction involving $-2e^-/-2H^+$ transfer, as observed in the potentiodynamic scans (Figure 1c,d). The two reduction steps, shown in Figure 3b, involve an initial reduction of C_1, in a $+1e^-/+1H^+$ process of high redox potential at the carbonyl oxygen to form a radical intermediate, which then faces another $+1e^-/+1H^+$ redox process to form the Alizarin Red S molecule. The second, low-potential, reduction of ARS at the carbonyl oxygen at C_{10}, strongly stabilized by resonance, sequentially drives the reduction of the radical intermediate at the carbonyl oxygen at C_9, affording the completely reduced form. Additionally, C−O bonds are strongly polarized toward oxygen (electronegativity of C = 2.55 vs that of O = 3.44) and are directly related to the C−O bond length. The four C═O double bonds at C_1, C_2, C_9, and C_{10} in the fully oxidized state are shorter (123 pm) than the 4 C−O single bonds at the same atoms (147 pm) in the fully reduced state. As a result, the C═O bonds in the oxidized form are more polarized toward the oxygens than the C−O bonds in the reduced one; consequently, the electronic density ($\delta-$) is more localized toward oxygen, deactivating the aromatic rings more ($\delta+$) and matching the results observed

https://doi.org/10.1021/acssuschemeng.3c08218
ACS Sustainable Chem. Eng. XXXX, XXX, XXX−XXX

in Figure 1f. The proposed mechanism provides evidence for the requirement of proper electrode design to stabilize the radicals, and especially, the deactivated and positive R3 ring.

Designing a Symmetric Quinone Aqueous Redox Flow Battery. Considering the previous conclusions, we employed electrode engineering to fabricate a SQA-RFB with HPCCE-5H as cathode and anode electrode materials. A porous cellulose separator was employed instead of an ion-exchange membrane. The separator was previously tested for ARS crossover (>24 h) under forced convection (see Figure S21). The potentials of each side of the battery, as well as the overall cell voltage, were continuously measured by real-time multipotentiometry monitoring (Figure 4a).

Although the HEDGE offers the best results to enable the high-potential redox pair reversibility, its application in a RFB hardware is not practicable. Therefore, we used HPCCE-5H, a carbon cloth, as the electrode material on both negative and positive sides. As on HEDGE, the fibers that form the carbon cloth display C═O and C−O groups on their surfaces after chemical oxidation treatment (see Section S1.3 in the Supporting Information). Additionally, it is a more robust material than the often-employed conducting carbon papers like SGL 39AA because the latter suffers from surface cracks and chemical modification, especially by operation at the negative electrode,[41] compromising the mechanical and chemical stabilities of the material in a short time span.[30] Thus, a SQA-RFB was assembled using ARS (10 mmol L^{-1} ARS in 1.0 mol L^{-1} H_2SO_4) as positive and negative electrolytes (Figure 4b,c), in the discharged state (ARS in a partially oxidized form).

Through multipotentiostatic real-time monitoring, we were able to fully investigate both negative and positive electrodes, as well as the entire battery, while the SQA-RFB was subjected to charge and discharge cycles. With that, the potential of the positive (E_+) and negative (E_-) electrodes could be measured separately and concomitantly to the cell voltage. After charging until reaching 50% state of charge, charge and discharge cycles were executed in the galvanostatic mode at a constant current of ±1.61 mA cm^{-2} and potential cutoffs equal to 0.0 and 1.2 V. The RFB cycling shown in Figure 4d implies that (i) separate and reversible defined Faradaic processes occurring at each electrode, (ii) a maximum cell voltage of ∼1 V represented by the difference between E_+ and E_- at the quasi-linear region ($dV/dC \approx 0$), (iii) lower voltages at the negative redox side suggest room for molecular engineering to enlarge the potential window and cell voltage, and (iv) there is a limiting negative electrode service range (blue dashed line) indicating partial loss of molecules after each oxidation at E_+, i.e., not all molecules oxidized are subsequently reduced; this comes from the fact that redox processes occur in a stable battery when a peak in differential capacity happens and when this parameter drops after the peak a new—parallel—process begins, such as solvent electrochemical decomposition; the dashed line corresponds to the potential of constant differential capacity; in summary, the negative side is limiting the battery due to material depletion (diffusion loss) that is lost at the positive side. Finally, (v) continuous capacity fading due to probable decomposition after the formation of the ARS fully oxidized form, also seen in Figure 4e. The internal resistance was measured as 0.44 Ω (see Figure S22).

In this study, new insights into the lack of stability of the fully oxidized state are achieved, which are shown to be responsible for the impossibility of developing SQA-RFBs to

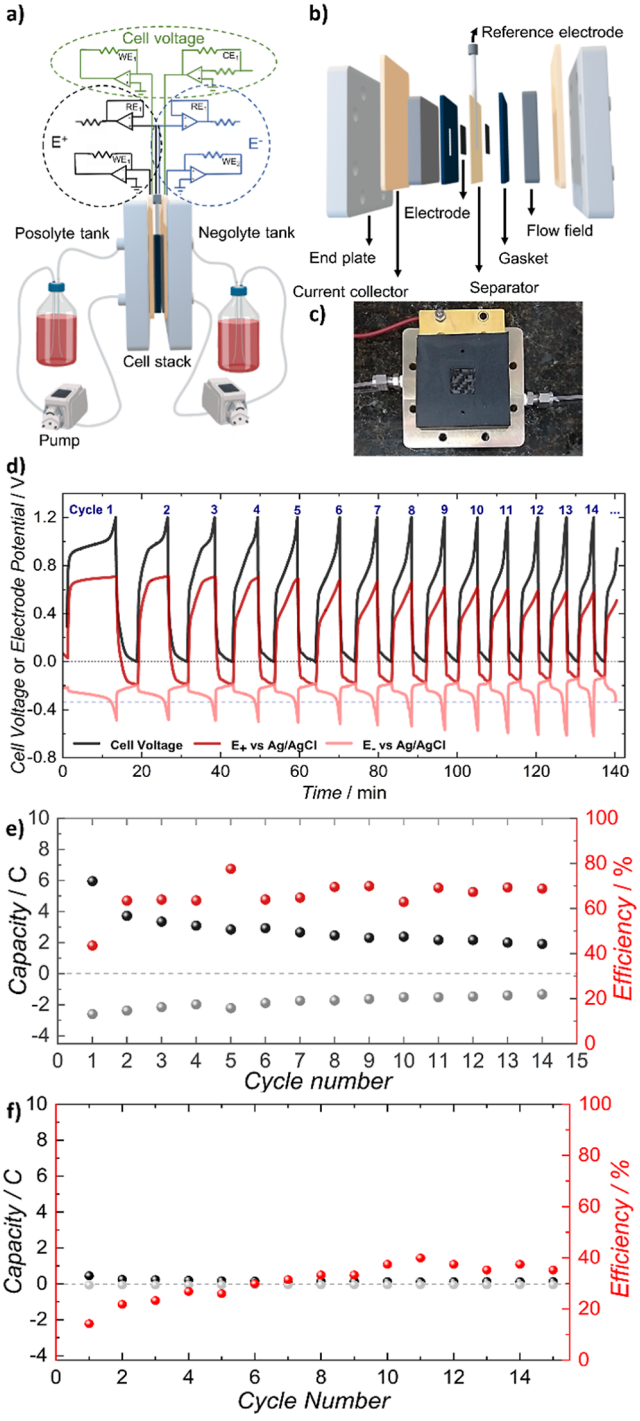

Figure 4. a) Schematic of the ARS symmetric RFB operated under galvanostatic regime and monitored with a multipotentiostatic real-time setup, with a single pseudoreference electrode at the separator as a common reference for both electrodes; ARS 10 mmol L^{-1} in 1.0 mol L^{-1} H_2SO_4 in both fluid compartments; (b) 3D schematic view of the cell assembly, comprising the electrodes and cellulose separator, identical flow fields, current collectors, and end plates; a pseudoreference electrode is also implemented, enabling the measurements of potentials relative to the respective electrode; and (c) half-cell photograph, with the HPCCE-5H fiber mesh positioned under the gasket frame (center). (d) Real-time and concomitant cell (black), negative (pink), and positive (red) electrode potential measurements during charge−discharge cycles at 1.61 mA cm^{-2} with the HPCCE-5H electrodes employed on both sides; the gray dotted line indicates 0 V for visual reference, and the blue dashed line points the low limit

https://doi.org/10.1021/acssuschemeng.3c08218
ACS Sustainable Chem. Eng. XXXX, XXX, XXX−XXX

Figure 4. continued

service potential range delimiting the overrun toward a parallel redox processes; cycle number on top, dark blue; cell voltage reported as a two-electrode configuration, while E_+ and E_- are reported versus the pseudoreference; (e) charge black (•) and discharge ash (•) capacities and Coulombic efficiency red (•) vs cycle number. (f) Charge and discharge capacities for the RFB without the electrostatic stabilization for comparison.

date. Here, the electrode engineering enabled the high-potential pair redox process to occur with higher reversibility, although in demanding forced mass-transfer conditions, the Coulombic efficiency is still refinable (≅ 65%, Figure 4e). The theoretical capacity for this battery is 38.60 C. The flow rate was previously optimized though a step potential polarization method (Figure S23).

For comparison, the performance of a RFB with bare HPCCE-5H electrodes without the electrostatic stabilization capability is also studied. The impedance spectroscopy result of two systems is shown in Figure S21, in which the electrode chemical treatment diminishes the resistance by ca. 2.3×, and the overall data suggests a much higher charge-transfer resistance without the surface stabilization. The charge−discharge from this system shown in Figure 4f depicts a ca. 10× reduced initial charging capacity with virtually zero discharge capacity compared to the RFB with the stabilization capability. The efficiency starts at 14.2% and raises to almost 40%; however, this is a mere artifact due to the almost constant discharge capacity values. These were at the minimal of the potentiostat sampling (difficulty to measure a smaller charge) combined with the diminishing charge capacity, leading to higher apparent values. The comparison of Figure 4e,f indicates how the stabilization effect enables the cyclability of the ARS from zero cycles to over 15 cycles despite the still improvable performance. Figures S24 and S25 show the cycle-per-cycle capacity loss for both systems and the $V-C$ curves, respectively.

Despite the prototype SQA-RFB still requiring future improvements for higher efficiency, the achieved stabilization of high-potential redox pairs promotes the first report of a cyclable RFB, with no other viable strategies shown to date. This opens room for exciting next steps in order to improve the system for operational applications.

CONCLUSIONS

In conclusion, this study provides insights into the electro-oxidation of ARS from its intermediate oxidation state to its highest oxidation state, proceeding by two distinct one-electron, one-proton processes, and the radical formed by the first such process is unstable. The mechanism is consistent with the results of electrochemical and in situ spectroelectrochemical measurements, further supported by DFT studies.

Installing carboxyl groups on carbonaceous electrodes greatly enhances the reversibility of the electrochemical oxidation of ARS to its highest oxidized state. Through DFT-generated MEPs, we show that the rings in the intermediate and fully oxidized states of ARS retain positive electrostatic charge, allowing their adsorption and stabilization by nucleophilic groups on the electrodes.

Furthermore, we report the first demonstration of a cyclable SQA-RFB with ARS in both electrolytes, separated by only a cellulose porous separator, and Faradaic processes driven on both sides by HPCCE-5H electrodes engineered to comprehend net negative charges needed for electrostatic stabilization.

Overall, this work highlights the importance of understanding molecular electrostatics and molecular stability during redox processes and electrode engineering to enhance stability in the design of future RFBs. This, thereby, opens vast possibilities for efficient, stable, and low-cost symmetric RFBs.

EXPERIMENTAL SECTION

Electrochemical analysis was performed employing an Autolab PGSTST128N (Metrohm), using Ag/AgCl/Cl^-_{sat} as the reference electrode and a Pt plate as the auxiliary electrode. Working electrodes consisted of Au disk, GCE, HEDGE, or HPCCE-5H fibers, following pretreatments as discussed in detail in the Supporting Information file. ARS solutions were characterized by NMR, and ARS solutions were filtered with a syringe filter to remove eventually insolubilized particles.

FTIR data was collected using a Bruker Vertex 70v spectrometer, with accumulation of 32 scans, 4 cm^{-1} resolution, and, for the in situ experiments, a 300 s stabilization time at each potential was used. Potentials ranged from −0.20 to +1.20 V in 1.0 mol L^{-1} H_2SO_4 containing 1.0 mmol L^{-1} ARS. See the Supporting Information file for additional information.

UV−vis spectroscopy was performed using a Jasco V-670 equipment in the range of 800−200 nm, with a 1 cm path length quartz cuvette; in situ experiments followed the same protocol described for the in situ FTIR.

The redox flow battery assessment was performed using a solution of 10 mmol L^{-1} ARS in 1 mol L^{-1} H_2SO_4 as an electrolyte in both compartments, a stack of 5 cm^2 treated (or untreated, for control experiments) HPCCE-5H fibers as electrodes for the anode and cathode, and a commercial cell with a serpentine flow field. Direct contact of redox species was prevented by using a simple dialysis separator. The measurement of each electrode potential as well as the overall battery potential difference was enabled due to an additional Ag/AgCl pseudoreference wire attached to the dialysis separator. Please check the Supporting Information file for additional information.

Computational modeling was performed using Gaussian 09 and Orca 4.2, and specifications of the molecules, calculations, and data analysis are discussed in the Supporting Information file.

ASSOCIATED CONTENT

Supporting Information

The Supporting Information is available free of charge at https://pubs.acs.org/doi/10.1021/acssuschemeng.3c08218.

^{1}H NMR spectra for purified ARS; experimental methods and details; materials; supporting electrochemical and spectroscopic data including CVs, DPVs, XPS, FTIR, UV−vis, DFT data, and EIS; and additional battery performance data (PDF)

AUTHOR INFORMATION

Corresponding Author

Frank Nelson Crespilho − *São Carlos Chemistry Institute, University of São Paulo, São Carlos, São Paulo 05508-220, Brazil; Harvard John A. Paulson School of Engineering and Applied Sciences, Cambridge, Massachusetts 02134, United States;* orcid.org/0000-0003-4830-652X; Email: frankcrespilho@iqsc.usp.br

Authors

José Eduardo dos Santos Clarindo − *São Carlos Chemistry Institute, University of São Paulo, São Carlos, São Paulo 05508-220, Brazil*

https://doi.org/10.1021/acssuschemeng.3c08218
ACS Sustainable Chem. Eng. XXXX, XXX, XXX−XXX

Rafael Neri Prystaj Colombo − *São Carlos Chemistry Institute, University of São Paulo, São Carlos, São Paulo 05508-220, Brazil;* orcid.org/0000-0001-8126-4398

Graziela Cristina Sedenho − *São Carlos Chemistry Institute, University of São Paulo, São Carlos, São Paulo 05508-220, Brazil; Harvard John A. Paulson School of Engineering and Applied Sciences, Cambridge, Massachusetts 02134, United States;* Present Address: Department of Chemistry, Federal University of São Carlos (UFSCar), São Carlos, SP, Brazil

Luana Cristina Italiano Faria − *São Carlos Chemistry Institute, University of São Paulo, São Carlos, São Paulo 05508-220, Brazil*

Thiago Bertaglia − *São Carlos Chemistry Institute, University of São Paulo, São Carlos, São Paulo 05508-220, Brazil;* orcid.org/0000-0001-8409-4734

Filipe Camargo Dalmatti Alves Lima − *Federal Institute of Education, Science, and Technology of São Paulo (IFSP), Matão, São Paulo 15991, Brazil;* orcid.org/0000-0001-7062-5450

Roberto da Silva Gomes − *Department of Pharmaceutical Sciences, College of Pharmacy, North Dakota State University, Fargo, North Dakota 58105, United States;* orcid.org/0000-0002-8075-9716

Michael J. Aziz − *Harvard John A. Paulson School of Engineering and Applied Sciences, Cambridge, Massachusetts 02134, United States;* orcid.org/0000-0001-9657-9456

Complete contact information is available at: https://pubs.acs.org/10.1021/acssuschemeng.3c08218

Author Contributions

F.N.C., M.J.A., and G.C.S. conceived the project. J.E.d.S.C., R.N.P.C., G.C.S., L.C.I.F., and T.B. performed the experiments; R.N.P.C. and F.C.D.A.L. ran the computational simulations and interpretation; and F.N.C. and R.d.S.G. developed the organic mechanism. All authors analyzed the data, wrote the manuscript, and contributed to the final version. R.N.P.C., G.C.S., and L.C.I.F. equally contributed to this work.

Funding

FAPESP, under the processes 2021/05665-7 (R.N.P.C.), 2017/15714-0, 2015/22973-6, and 2020/04796-8 (G.C.S), 2019/12053-8, 2019/15333-1, 2018/22214-6, and 2022/09164-5 (F.N.C.), 2019/21089-6 and 2021/14537-2 (L.C.I.F.), 2020/03681-2 (T.B.), 2023/17506-6 (F.C.D.A.L.). CNPq, under processes 428211/2018-6 (F.C.D.A.L.) and 203299/2017-5 (F.N.C). CAPES under process PROEX 1806336 (J.E.d.S.C.).

Funding

The Article Processing Charge for the publication of this research was funded by the Coordination for the Improvement of Higher Education Personnel - CAPES (ROR identifier: 00x0ma614).

Notes

The authors declare no competing financial interest.

ACKNOWLEDGMENTS

Authors acknowledge The São Paulo Research Foundation FAPESP and the Brazilian National Council for Scientific and Technological Development (CNPq) for the fundings provided. The computational time was provided by resources supplied by the USP-HPC, CENAPAD/SP, and IFSP. Authors thank Yan Jing for the mechanism drawing revision.

ABBREVIATIONS

ARS, alizarin red S; CV, cyclic voltammetry; cys, cysteamine; DFT, density functional theory; DPV, differential pulse voltammetry; FTIR, Fourier transform infrared spectroscopy; GCE, glassy carbon electrode; HEDGE, high-edge-density graphite electrode; H/L, HOMO/LUMO; MEP, molecular electrostatic potential map; MO, molecular orbital; MWCNT, multiwalled carbon nanotubes; RFB, redox flow battery; SOC, state of charge; SQA-RFB, symmetric quinone aqueous redox flow battery; TD-DFT, time-domain density functional theory; XPS, X-ray photoelectron spectroscopy

REFERENCES

(1) Lowe, R. J.; Drummond, P. Solar, Wind and Logistic Substitution in Global Energy Supply to 2050—Barriers and Implications. *Renewable Sustainable Energy Rev.* **2022**, *153*, 111720.

(2) Tatar, S. M.; Akulker, H.; Sildir, H.; Aydin, E. Optimal Design and Operation of Integrated Microgrids under Intermittent Renewable Energy Sources Coupled with Green Hydrogen and Demand Scenarios. *Int. J. Hydrogen Energy* **2022**, *47* (65), 27848−27865.

(3) Dunn, B.; Kamath, H.; Tarascon, J.-M. Electrical Energy Storage for the Grid: A Battery of Choices. *Science* **2011**, *334* (6058), 928−935.

(4) Potash, R. A.; McKone, J. R.; Conte, S.; Abruña, H. D. On the Benefits of a Symmetric Redox Flow Battery. *J. Electrochem. Soc.* **2016**, *163* (3), A338−A344.

(5) Wu, C.; Zhang, X.-P.; Sterling, M. Solar Power Generation Intermittency and Aggregation. *Sci. Rep.* **2022**, *12* (1), 1363.

(6) Colombo, R. N. P.; Sedenho, G. C.; Crespilho, F. N. Challenges in Biomaterials Science for Electrochemical Biosensing and Bioenergy. *Chem. Mater.* **2022**, *34*, 10211−10222.

(7) Alotto, P.; Guarnieri, M.; Moro, F. Redox Flow Batteries for the Storage of Renewable Energy: A Review. *Renewable Sustainable Energy Rev.* **2014**, *29*, 325−335.

(8) Sánchez-Díez, E.; Ventosa, E.; Guarnieri, M.; Trovò, A.; Flox, C.; Marcilla, R.; Soavi, F.; Mazur, P.; Aranzabe, E.; Ferret, R. Redox Flow Batteries: Status and Perspective towards Sustainable Stationary Energy Storage. *J. Power Sources* **2021**, *481*, 228804.

(9) Skyllas-Kazacos, M.; Grossmith, F. Efficient Vanadium Redox Flow Cell. *J. Electrochem. Soc.* **1987**, *134* (12), 2950−2953.

(10) Huskinson, B.; Marshak, M. P.; Suh, C.; Er, S.; Gerhardt, M. R.; Galvin, C. J.; Chen, X.; Aspuru-Guzik, A.; Gordon, R. G.; Aziz, M. J. A Metal-Free Organic-Inorganic Aqueous Flow Battery. *Nature* **2014**, *505* (7482), 195−198.

(11) Lin, K.; Chen, Q.; Gerhardt, M. R.; Tong, L.; Kim, S. B.; Eisenach, L.; Valle, A. W.; Hardee, D.; Gordon, R. G.; Aziz, M. J.; Marshak, M. P. Alkaline Quinone Flow Battery. *Science* **2015**, *349*, 1529−1532.

(12) Asenjo-Pascual, J.; Salmeron-Sanchez, I.; Avilés-Moreno, J. R.; Mauleón, P.; Mazur, P.; Ocón, P. Understanding Aqueous Organic Redox Flow Batteries: A Guided Experimental Tour from Components Characterization to Final Assembly. *Batteries* **2022**, *8* (10), 193.

(13) Haisch, T.; Ji, H.; Weidlich, C. Monitoring the State of Charge of All-Vanadium Redox Flow Batteries to Identify Crossover of Electrolyte. *Electrochim. Acta* **2020**, *336*, 135573.

(14) Chou, Y.-S.; Yen, S.-C.; Arpornwichanop, A.; Singh, B.; Chen, Y.-S. Mathematical Model to Study Vanadium Ion Crossover in an All-Vanadium Redox Flow Battery. *ACS Sustainable Chem. Eng.* **2021**, *9* (15), 5377−5387.

(15) Yao, Y.; Lei, J.; Shi, Y.; Ai, F.; Lu, Y.-C. Assessment Methods and Performance Metrics for Redox Flow Batteries. *Nat. Energy* **2021**, *6* (6), 582−588.

(16) Symons, P. Quinones for Redox Flow Batteries. *Curr. Opin. Electrochem.* **2021**, *29*, 100759.
(17) Gerhardt, M. R.; Tong, L.; Gómez-Bombarelli, R.; Chen, Q.; Marshak, M. P.; Galvin, C. J.; Aspuru-Guzik, A.; Gordon, R. G.; Aziz, M. J. Anthraquinone Derivatives in Aqueous Flow Batteries. *Adv. Energy Mater.* **2017**, *7* (8), 1601488.
(18) Tabor, D. P.; Gómez-Bombarelli, R.; Tong, L.; Gordon, R. G.; Aziz, M. J.; Aspuru-Guzik, A. Mapping the Frontiers of Quinone Stability in Aqueous Media: Implications for Organic Aqueous Redox Flow Batteries. *J. Mater. Chem. A* **2019**, *7* (20), 12833−12841.
(19) Fornari, R. P.; Mesta, M.; Hjelm, J.; Vegge, T.; de Silva, P. Molecular Engineering Strategies for Symmetric Aqueous Organic Redox Flow Batteries. *ACS Mater. Lett.* **2020**, *2* (3), 239−246.
(20) Li, M.; Case, J.; Minteer, S. D. Bipolar Redox-Active Molecules in Non-Aqueous Organic Redox Flow Batteries: Status and Challenges. *ChemElectroChem* **2021**, *8* (7), 1215−1232.
(21) Liu, B.; Tang, C. W.; Sheong, F. K.; Jia, G.; Zhao, T. Artificial Bipolar Redox-Active Molecule for Symmetric Nonaqueous Redox Flow Batteries. *ACS Sustainable Chem. Eng.* **2022**, *10* (1), 613−621.
(22) Liu, Y.; Dai, G.; Chen, Y.; Wang, R.; Li, H.; Shi, X.; Zhang, X.; Xu, Y.; Zhao, Y. Effective Design Strategy of Small Bipolar Molecules through Fused Conjugation toward 2.5 V Based Redox Flow Batteries. *ACS Energy Lett.* **2022**, *7* (4), 1274−1283.
(23) Steen, J. S.; Nuismer, J. L.; Eiva, V.; Wiglema, A. E. T.; Daub, N.; Hjelm, J.; Otten, E. Blatter Radicals as Bipolar Materials for Symmetrical Redox-Flow Batteries. *J. Am. Chem. Soc.* **2022**, *144* (11), 5051−5058.
(24) Tong, L.; Jing, Y.; Gordon, R. G.; Aziz, M. J. Symmetric All-Quinone Aqueous Battery. *ACS Appl. Energy Mater.* **2019**, *2* (6), 4016−4021.
(25) Kwabi, D. G.; Ji, Y.; Aziz, M. J. Electrolyte Lifetime in Aqueous Organic Redox Flow Batteries: A Critical Review. *Chem. Rev.* **2020**, *120* (14), 6467−6489.
(26) Sedenho, G. C.; De Porcellinis, D.; Jing, Y.; Kerr, E.; Mejia-Mendoza, L. M.; Vazquez-Mayagoitia, A. ́.; Aspuru-Guzik, A.; Gordon, R. G.; Crespilho, F. N.; Aziz, M. J. Effect of Molecular Structure of Quinones and Carbon Electrode Surfaces on the Interfacial Electron Transfer Process. *ACS Appl. Energy Mater.* **2020**, *3* (2), 1933−1943.
(27) Amiri, H.; Khosravi, M.; Ejeian, M.; Razmjou, A. Designing Ion-Selective Membranes for Vanadium Redox Flow Batteries. *Adv. Mater. Technol.* **2021**, *6* (10), 2001308.
(28) Mukhopadhyay, A.; Cheng, Z.; Natan, A.; Ma, Y.; Yang, Y.; Cao, D.; Wang, W.; Zhu, H. Stable and Highly Ion-Selective Membrane Made from Cellulose Nanocrystals for Aqueous Redox Flow Batteries. *Nano Lett.* **2019**, *19* (12), 8979−8989.
(29) Pereira, A. R.; de Souza, J. C. P.; Iost, R. M.; Sales, F. C. P. F.; Crespilho, F. N. Application of Carbon Fibers to Flexible Enzyme Electrodes. *J. Electroanal. Chem.* **2016**, *780*, 396−406.
(30) Faria, L. C. I.; Sedenho, G. C.; Bertaglia, T.; Macedo, L. J. A.; Crespilho, F. N. A Comparative Study of Chemically Oxidized Carbon Cloth and Thermally Treated Carbon Paper Electrodes Applied on Aqueous Organic Redox Flow Batteries. *Electrochim. Acta* **2024**, *485*, 144086.
(31) Laviron, E. The Use of Linear Potential Sweep Voltammetry and of a.c. Voltammetry for the Study of the Surface Electrochemical Reaction of Strongly Adsorbed Systems and of Redox Modified Electrodes. *J. Electroanal. Chem. Interfacial Electrochem.* **1979**, *100* (1−2), 263−270.
(32) Han, C.; Li, H.; Shi, R.; Zhang, T.; Tong, J.; Li, J.; Li, B. Organic Quinones towards Advanced Electrochemical Energy Storage: Recent Advances and Challenges. *J. Mater. Chem. A* **2019**, *7* (41), 23378−23415.
(33) Bachman, J. E.; Curtiss, L. A.; Assary, R. S. Investigation of the Redox Chemistry of Anthraquinone Derivatives Using Density Functional Theory. *J. Phys. Chem. A* **2014**, *118* (38), 8852−8860.
(34) Ossowski, T.; Pipka, P.; Liwo, A.; Jeziorek, D. Electrochemical and UV-Spectrophotometric Study of Oxygen and Superoxide Anion Radical Interaction with Anthraquinone Derivatives and Their Radical Anions. *Electrochim. Acta* **2000**, *45* (21), 3581−3587.
(35) Gadre, S. R.; Suresh, C. H.; Mohan, N. Electrostatic Potential Topology for Probing Molecular Structure, Bonding and Reactivity. *Molecules* **2021**, *26* (11), 3289.
(36) Ninković, D. B.; BlagojevićFilipović, J. P.; Hall, M. B.; Brothers, E. N.; Zarić, S. D. What Is Special about Aromatic-Aromatic Interactions? Significant Attraction at Large Horizontal Displacement. *ACS Cent. Sci.* **2020**, *6* (3), 420−425.
(37) Machado, F. M.; Carmalin, S. A.; Lima, E. C.; Dias, S. L. P.; Prola, L. D. T.; Saucier, C.; Jauris, I. M.; Zanella, I.; Fagan, S. B. Adsorption of Alizarin Red S Dye by Carbon Nanotubes: An Experimental and Theoretical Investigation. *J. Phys. Chem. C* **2016**, *120* (32), 18296−18306.
(38) Sedenho, G. C.; Hassan, A.; Souza, J. C. P. D.; Crespilho, F. N. In Situ and Operando Electrochemistry of Redox Enzymes. *Curr. Opin. Electrochem.* **2022**, *34*, 101015.
(39) de Souza, J. C. P.; Macedo, L. J. A.; Hassan, A.; Sedenho, G. C.; Modenez, I. A.; Crespilho, F. N. In Situ and Operando Techniques for Investigating Electron Transfer in Biological Systems. *ChemElectroChem* **2021**, *8* (3), 431−446.
(40) Jones, A. E.; Ejigu, A.; Wang, B.; Adams, R. W.; Bissett, M. A.; Dryfe, R. A. W. Quinone Voltammetry for Redox-Flow Battery Applications. *J. Electroanal. Chem.* **2022**, *920*, 116572.
(41) Singh, A. K.; Pahlevaninezhad, M.; Yasri, N.; Roberts, E. P. L. Degradation of Carbon Electrodes in the All-Vanadium Redox Flow Battery. *ChemSusChem* **2021**, *14* (9), 2100−2111.

https://doi.org/10.1021/acssuschemeng.3c08218
ACS Sustainable Chem. Eng. XXXX, XXX, XXX−XXX

Supporting Information

Molecular Mechanism and Electrostatic Effect Enabling Symmetric All-Quinone Aqueous Redox Flow Battery

José Eduardo dos Santos Clarindo[1]; Rafael Neri Prystaj Colombo[1†]; Graziela Cristina Sedenho[1,4,5†]; Luana Cristina Italiano Faria[1,4†]; Thiago Bertaglia[1]; Filipe Camargo Dalmatti Alves Lima[2]; Roberto da Silva Gomes[3]; Michael J. Aziz;[4] Frank Nelson Crespilho[1,4*]

1 São Carlos Institute of Chemistry, University of São Paulo, São Carlos, SP, Brazil.

2 Federal Institute of Education, Science, and Technology of São Paulo (IFSP), Matão, SP, Brazil.

3 Department of Pharmaceutical Sciences, College of Pharmacy, North Dakota State University, Fargo, ND, United States.

4 Harvard John A. Paulson School of Engineering and Applied Sciences, Cambridge, MA, United Stated.

5 Current address: Department of Chemistry, Federal University of São Carlos (UFSCar), São Carlos, SP, Brazil.

† Equally contributed to this work

Contents

S1. Experimental section

S1.1. Materials and reagents

ARS, multi-walled carbon nanotube carboxylic acid-functionalized (MWCNT, >8% carboxylic acid-functionalized, average diameter: 9.5 nm, length: 1.5 µm, carbon content >80%), isopropanol (C_3H_8O, 60.10 g mol^{-1}, ≥99.5%), hydrochloric acid (HCl, 36.46 g mol^{-1}, 37%), and cysteamine (C_2H_7NS, 77.15 g mol^{-1}, 95%) were purchased Sigma-Aldrich®. ARS was previously purified as described in Section 1.2. Sulfuric acid (H_2SO_4, 96-98% *v/v*) and sodium permanganate ($KMnO_4$, 158.034 g mol^{-1}, 99.0%) were obtained from Qhemis® (H_2SO_4, 98.08 g mol^{-1}, 96-98%). All solutions were prepared with ultrapure water (18 MΩ cm at 25 °C) obtained from Direct Q®3 water purification system (Merckmillipore). HPCCE-5H was purchased from Delpho (Brazil), GCE (0.07 cm^2) and Au disk electrode (0.07 cm^2) were purchased from Metrohm (Swiss).

S1.2. ARS Purification

ARS was previously purified by sublimation. 2.0 g ARS was dissolved in 100 mL water/ethanol (1:1, v/v) and heated to 300° C under vacuum in a crucible dish. By controlling the temperature along the tube length, possible contaminant compounds were completely pumped out of the system. Then, the system was cooled to deposit the ARS and the purified compound was collected from the cooling surface.

All NMR data was obtained using a 500 MHz Agilent Instruments 500/54 Premium Shielded equipment, with a conventional 5 mm diameter probe, using 10 µL TMS for calibration (δ = 0.00 ppm). Purified ARS was analyzed by ^{1}H NM in deuterated DMSO (**Figure S1a-b**). The most defined singlet at 7.88 ppm is attributed to the proton attached to C4. The protons bonded to C5 and C8 are coupled to a neighboring proton each, generating two doublets resting in a similar chemical environment, therefore, with identical signals – two doublets close to 8.2 ppm. The same occurs with protons associated with C6 and C7 carbons, once again in similar chemical environments, however, each being coupled to two neighboring protons, resulting in a multiplet with a Pascal triangle shape at 7.92 ppm. These

results were also compared to DFT calculations (**Figure S1c**), showing the similar attribution. However, these theoretical peaks presented a global chemical shift of 1 ppm in average compared to the experimental spectrum.

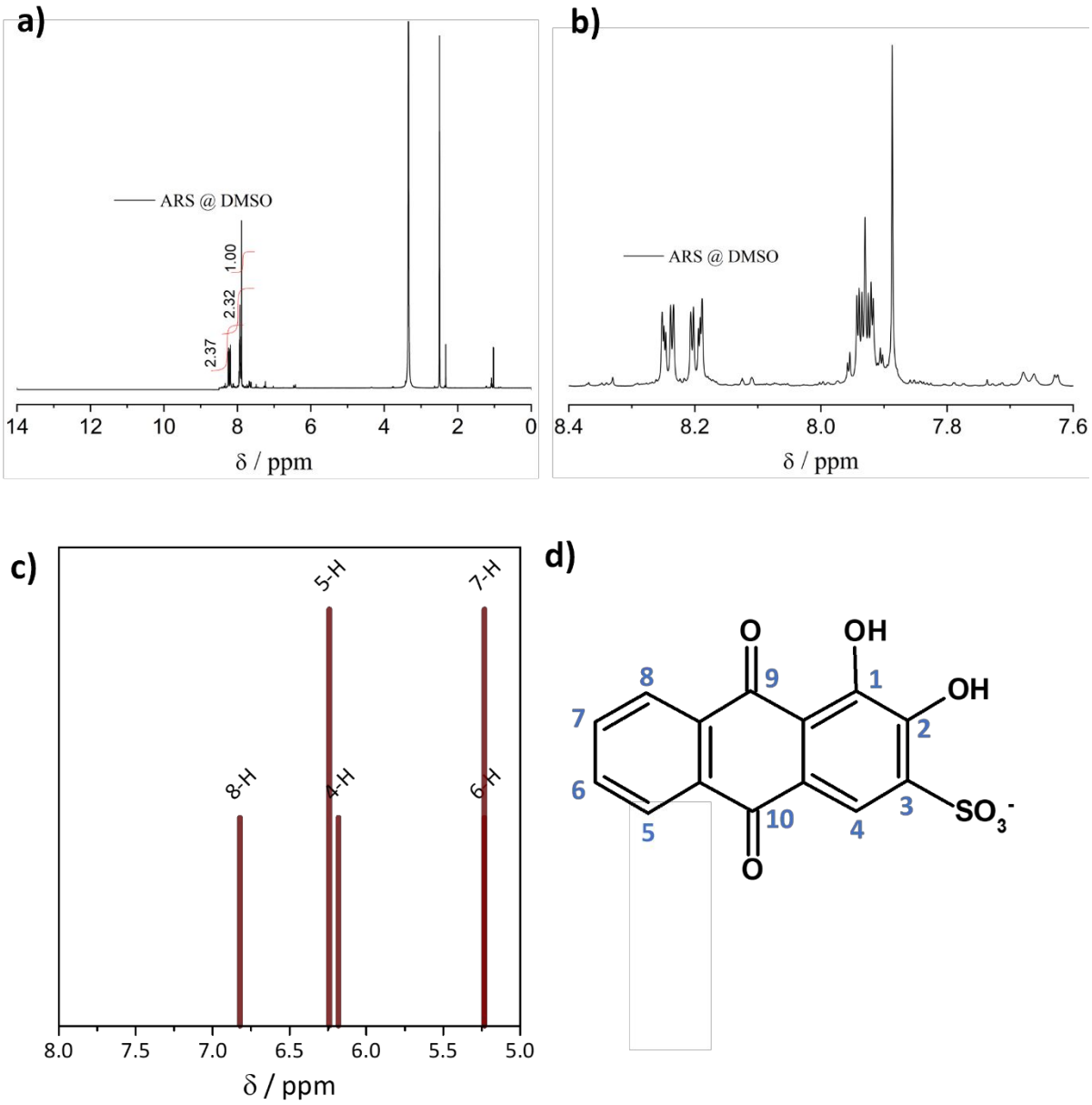

Figure S1. (a) ^{1}H NMR spectrum of purified ARS (partially oxidized state) in DMSO and its zoomed view (b). (c) ^{1}H NMR spectrum of ARS predicted by DFT. (d) ARS chemical structure with labeled carbon atoms.

S1.3. Half-cell electrochemical measurements

Cyclic voltammetry (CV) and chronoamperometry (CA) were carried out with a Potentiostat/Galvanostat Autolab PGSTAT 128N (Metrohm®) coupled to a microcomputer and controlled by NOVA 1.11 software. All measurements were performed using a three-electrode conventional cell using a platinum plate and an $Ag/AgCl/Cl^-_{sat}$ as counter and reference electrodes, respectively.

All experiments were carried out at room temperature and in an N_2 atmosphere, purged in solution for at least 10 min prior to the measurements. GCE, HEDGE, Au disk, Au/cys/MWCNT, and HPCCE-5H were used as working electrodes and prepared as follows: GCE was cleaned by polishing in 0.05 µm alumina slurry and then sonicated in deionized water for 5 min. HEDGE was prepared as previously described by manually polishing a graphite rod with a diameter of 6.1 mm on a DOBLE A ACB62 abrasive sheet with granulation of 2500 at an inclination of approximately 45^o.[1]

After the polishing, the electrode surface was washed with deionized water to remove the unattached particles. The HEDGE area was delimited by nitrocellulose resin to expose only the polished face with edge planes to the electrolyte.

For the gold modified with cysteamine and multiwalled carbon nanotubes, named Au/cys/MWCNT, a gold disk electrode was cleaned by polishing with 0.05 µm alumina slurry and sonicated in deionized water for 5 min; a cyclic voltammogram in sulfuric acid indicated surface cleanliness. In sequence, the electrode was immersed in a 20 mM cysteamine ethanolic solution for at least 30 min to coat the electrode through gold-thiol bonds. The electrode was then rinsed with deionized water, and a 10 µL droplet of MWCNT (2.2 mg/mL in 1:1 water/isopropanol) was added and let dry under vacuum.

HPCCE-5H was chemically treated as previously described.[2] HPCCE-5H was sonicated for 3 h in 1.0 mol L^{-1} H_2SO_4 containing 25 mmol L^{-1} $KMnO_4$. Then, the electrode was rinsed with HCl to remove the MnO_2 residues produced and followed by rinsing in deionized water to remove all the acid residues.

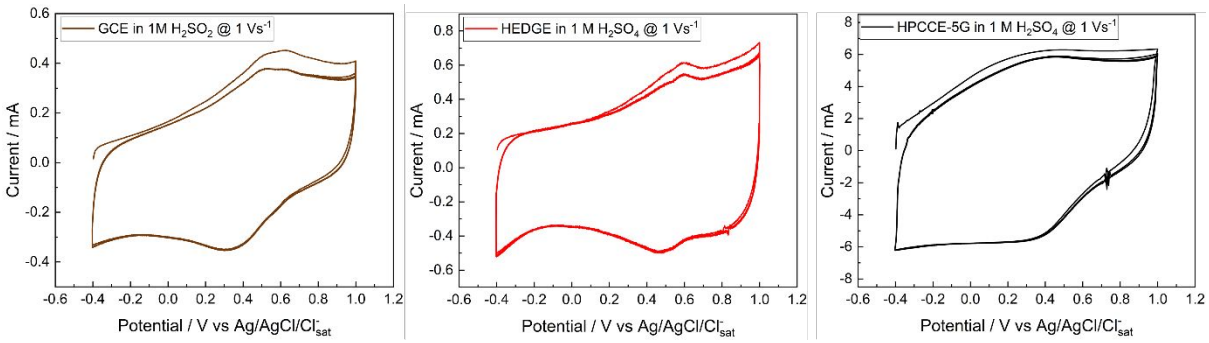

Figure S2. Cyclic voltammograms of GCE (left, brown), HEDGE (middle, red) and HPCCE-5H (right, black) in 1.0 mol L^{-1} H_2SO_4 electrolyte without ARS; collected at 1 V s^{-1} with iR-drop correction.

S1.4. XPS measurements

X-ray photoelectron spectroscopy (XPS) was used to determine the surface composition of pristine and treated HPCCE-5H samples. The analyses were performed on a Scienta-Omicron ECSA+ with a monochromatic Al Kα source, with a chamber pressure of 8×10^{-8} mbar. The O 1s high-resolution spectra of the pristine and treated HPCCE-5H electrodes were collected with a resolution of 0.05 eV. The Shirley function was used to determine the background subtraction of each spectrum and the Voigt-type function was used for the deconvolution.

S1.5. In situ and ex situ vibrational spectroscopy

FTIR spectra were recorded in a Vertex 70v FTIR spectrometer (Bruker). Each spectrum results from 32 scans with a spectral resolution of 4 cm^{-1}. FTIR spectrum on ATR mode of the solid ARS is shown in **Figure S16**. The assignment of the main vibrational modes is shown in **Table S2**. The in situ vibrational spectra were collected on reflection mode after 300 s of application of different electrochemical potentials ranging from -0.20 V to 1.20 V (*vs.* $Ag/AgCl_{sat}$) on polycrystalline Au disk working electrode in 1.0 mol L^{-1} H_2SO_4 containing 0.1 mmol L^{-1} ARS. All the measurements were performed in triplicate at room temperature and N_2 atmosphere. HPCCE-5H FTIR spectra were collected on ATR mode with a spectral resolution of 4 cm^{-1} and 32 scans.

S1.6. Redox flow battery measurements

For SQA-RFB measurements, 10.0 mmol L^{-1} ARS in 1.0 mol L^{-1} H_2SO_4 and a stack of 4 sheets of treated HPCCE-5H electrodes (geometric area = 5 cm^2 each) were used on both sides of the cell. A serpentine flow field was employed. A dialysis separator (0.26 mm, 3 kDa cut-off) was employed as a separator to prevent the mixing of the molecules in each redox state. Prior to use, the dialysis separator kept in ethanol (20% v/v) was rinsed with ultrapure water and soaked in 1.0 mol L^{-1} H_2SO_4 overnight. To analyze the separator crossover rate, the RFB was assembled as usual, however, one electrolyte compartment contained 10.0 mmol L^{-1} ARS in 1.0 mol L^{-1} H_2SO_4 and the other contained only 1.0 mol L^{-1} H_2SO_4; the pump was turned on (14.3 mL min^{-1}) and after 24h the electrolyte initially without ARS was studied though electronic spectroscopy, as in **Figure S19**. A set of dilutions was required for the ARS sample

due to the high optical absorptivity, in which the reference was collected at 60X, 90X, 120X and 180X dilutions, as well as in absence of ARS (zero concentration), and spectra were collected with a 1 cm optical pathway cuvette, from 300 nm to 800 nm, 2 nm bandwidth, 200 nm/min, single-scan, background subtracted. The charge and discharge cycling in the SQA-RFB was performed in galvanostatic mode with a constant current of ± 1.61 mA cm^{-2}, using voltage cut-offs of 0.0 V and 1.2V. Coupled with this analysis, an Ag/AgCl pseudo-reference electrode was interspersed between the HPCCE-5H electrodes and the dialysis separator to record the potential of each electrode simultaneously to the overall cell voltage.

S1.7. Computational Methods

Theoretical modeling was designed using Kohn-Sham's Density Functional Theory[3,4] as implemented in Gaussian 09[5] and ORCA 4.2.0.[6] The molecular models were designed at the total charge state -1 since the sulfonic group was deprotonated. The structures were fully optimized, thus minimizing the Hellman-Feynman forces at the default threshold in all cases. The vibrational study was carried out using Gaussian 09, with the exchange-correlation functional B3LYP[7] and Pople's polarized split-valence double-zeta basis set, 6-311G(d,p), basis set. The thermal effects were set at 300 K and vacuum conditions, i.e. no solvation. It was not observed any negative frequency for the cases investigated here. Moreover, TD-DFT[8,9] study was carried out using Gaussian 09, with the following configuration: basis set 6-31G(d,p); exchange-correlation B3LYP; first 40 transition states window; absence of temperature or solvent effects. For the chemical shifts ^{1}H NMR study, it was employed the basis set 6-31++G(d,p), including two diffuse functions for the heavy atoms and the Gauge Including Atomic Orbitals (GIAO) method.[10] The DMSO reference was obtained from using the improved aug-cc-pvdz basis set, obtaining a chemical shift reference of 29 ppm. Molecular electrostatic potential (MEP) maps were generated using ORCA 4.2.0, the exchange-correlation functional PBE0,[11] Ahlrichs TZVP basis set; the surface was plotted through a superposition of ionic densities at isosurface of 0.03. For uniformization, the same color scale was used to depict the most negatively charged spots (red, -0.075) and positively charged spots (blue, +0.075), with white denoting central values and, therefore, most charge-neutral regions.

S2. Differential pulse voltammetry

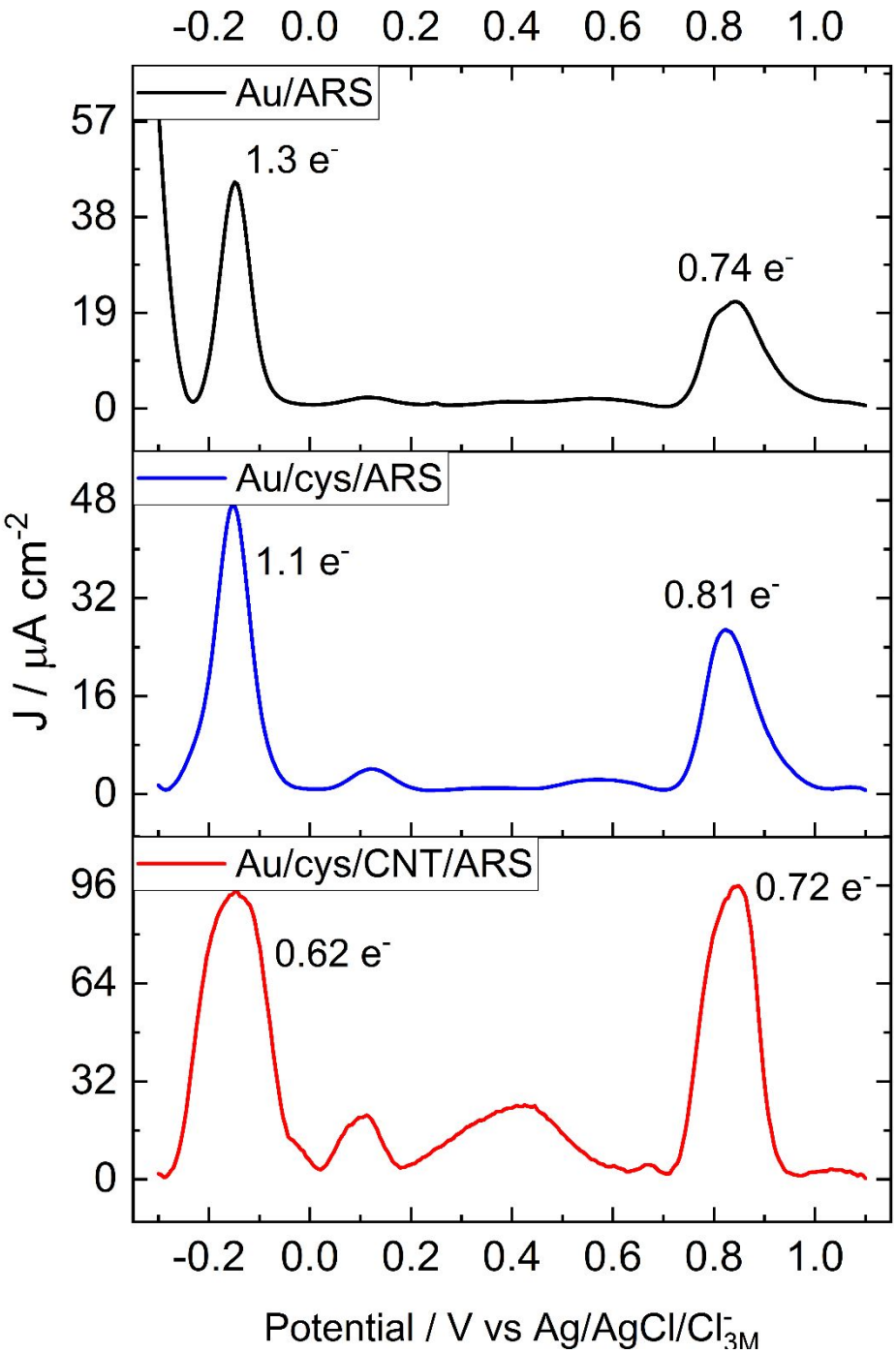

Figure S3. Differential pulse voltammetric (DPV) curves of ARS at Au (upper, black), Au-cysteamine (middle, blue) and Au-cysteamine-MWCNT (lower, red) electrodes. The number of electrons involved in each peak is roughly estimated through the Brumleve-Osteryoung models and is closer to unity, with distortions at the high-potential redox pair. The DPVs were performed from -0.3 to 1.1 V with 5 mV steps, 25 mV amplitude, 50 milliseconds of modulation, and 500 milliseconds of interval time. The presence of oxidized groups induces

the stabilization of intermediate states, as clearly seen in the bottom curve, at ca. 0.1 V and 0.4 V, similarly to the observed with fast-scan CVs.

S3. Engineering a carbon cloth electrode for SQA-RFB

The oxidative chemical treatment of carbon cloth electrode (HPCEE-5H, Delpho) with $KMnO_4$ in H_2SO_4, as described in Section 1.3, promotes the increase of structural defects and quinone functional groups on carbon fiber. In addition, the high-resolution XPS (pristine fiber, **Figure S5**, compared to **Figure 2a**) shows an increase in the oxygen-functional groups on the electrode surface with the chemical treatment, as expected and discussed elsewhere.[12] Pristine HPCCE-5H spectrum shows only one band at 532.1 eV attributed to C-O groups, whereas the spectrum of the treated electrode presents two bands, at 531.4 and 532.1 eV, assigned to C=O and C-O groups, respectively. This corroborates the presence of quinone functional groups on the carbon cloth induced by the chemical oxidative treatment.[13,14]

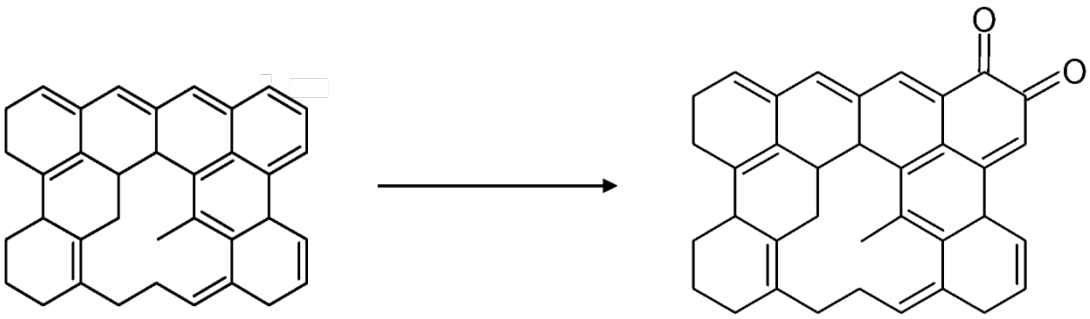

Figure S4. Oxidative chemical treatment of HPPCE-5H.

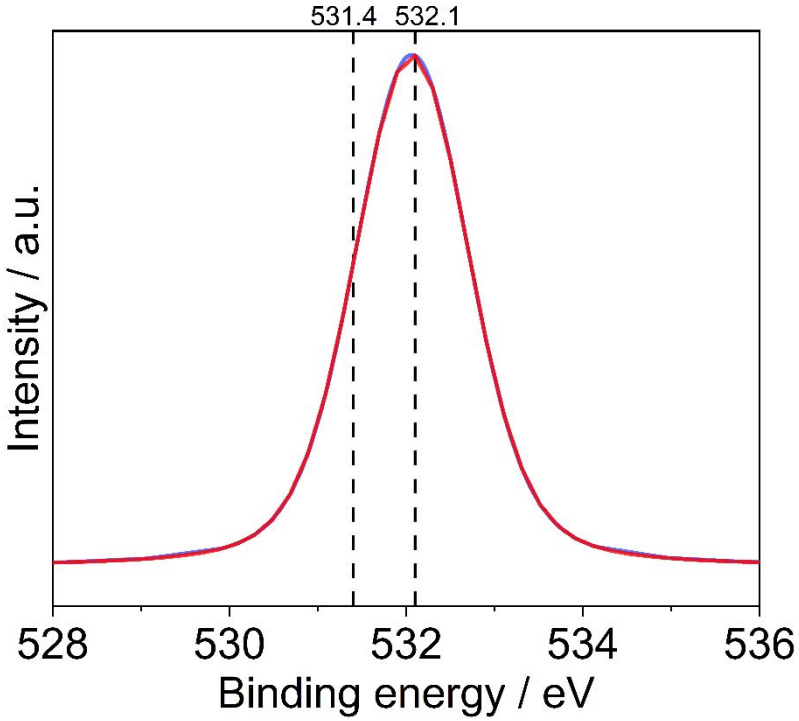

Figure S5. High-resolution O 1s XPS spectra of pristine HPCCE-5H. Red curve shows the raw spectrum, and the blue curve shows the deconvoluted curve.

S4. Micromolar regime electrochemistry

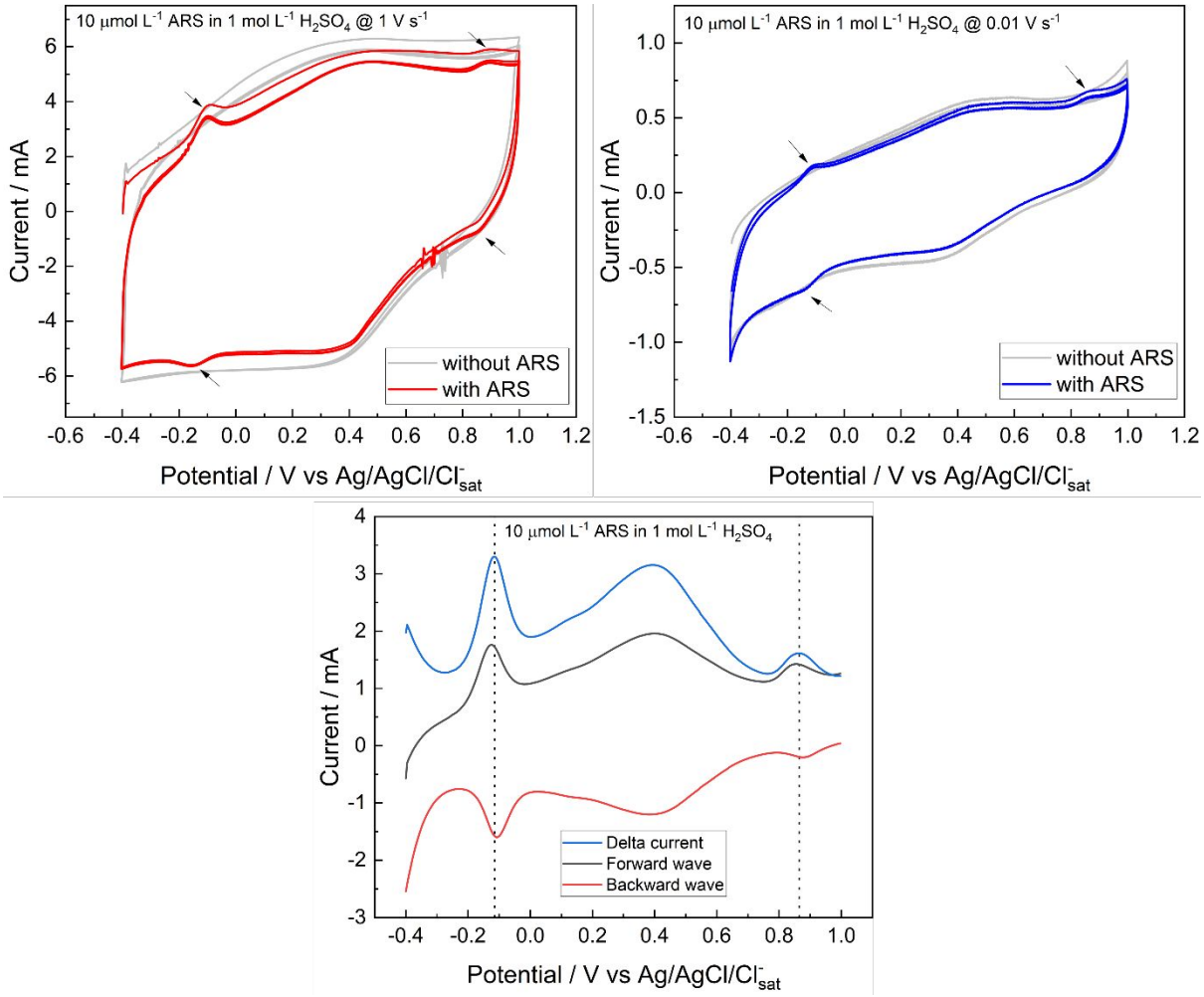

Figure S6. Cyclic voltammograms of a dilute 10 µM ARS in 1 M H_2SO_4 at 1 V s^{-1} (upper left) and 10 mV s^{-1} (upper right), highlighting the redox processes under an unfavorable mass transport condition; (lower) a Square Wave Voltammogram (SWV) split into the forward, backward and delta waves is shown indicating the reversibility of both the low potential and high potential redox pairs at the HPCCE-5H surface. All data recorded with iR-drop correction.

S4. Calculation of ARS rate constant by Laviron method

The electrochemical redox reactions of the adsorbed ARS molecules on the GCE and HPCCE-5H electrodes were investigated in 1.0 mol L^{-1} H_2SO_4 at different scan rates ranging from 0.005 V s^{-1} to 5 V s^{-1}, as shown in (**Figure S7a-b**). An increase in the peak current densities current is observed concomitantly with the increase in the scan rate. **Figures S7c-f** show linear dependencies of the current densities of the anodic (j_{pa}) and cathodic (j_{pc}) peaks as a function of

the scan rate (*v*) for GCE and HPCEE-5H electrodes, indicating that the electrochemical processes are governed by the transfer of electrons at the solution–electrode interface.

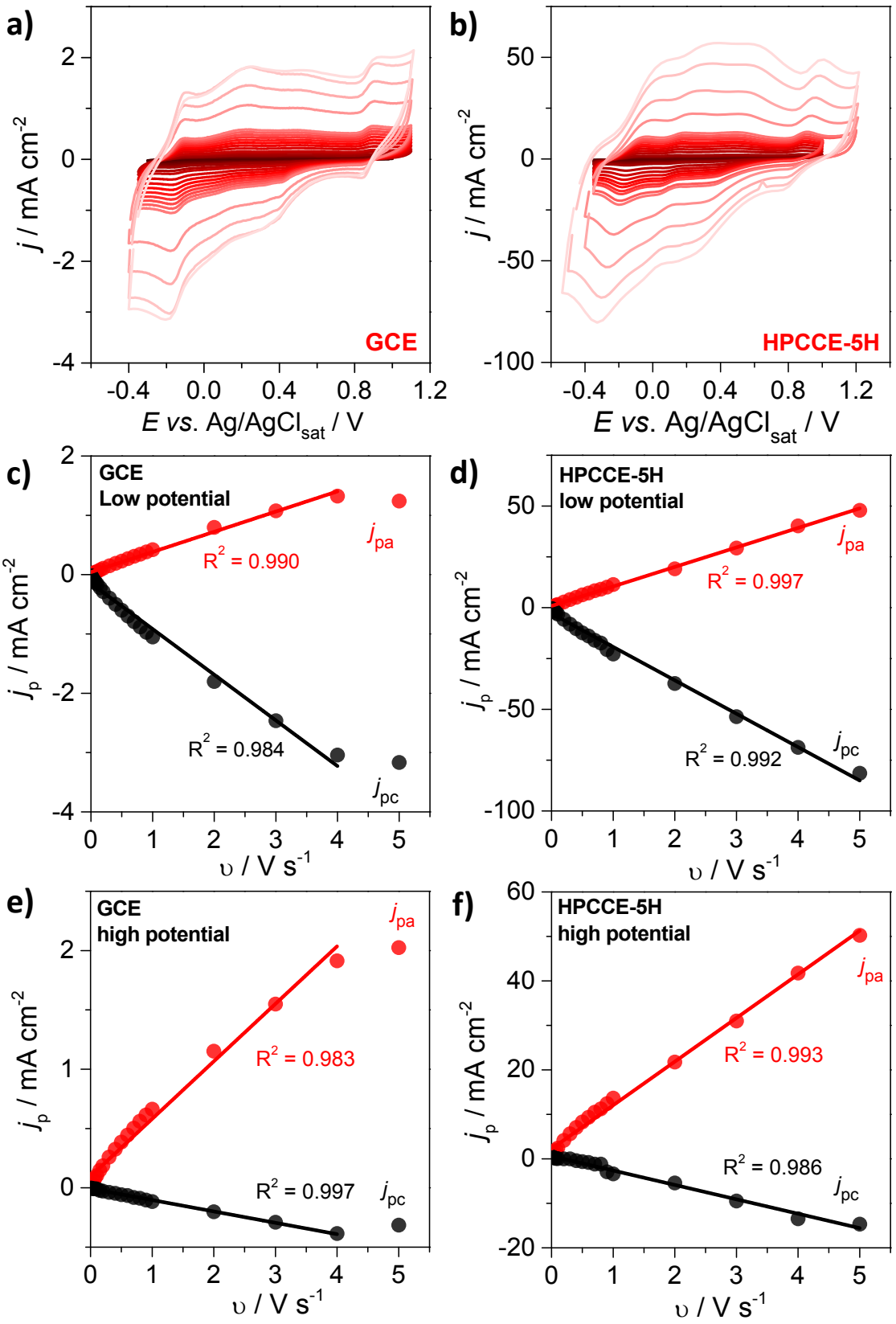

Figure S7. Cyclic voltammograms recorded at different scan rates from 0.005 to 5 V s^{-1} with adsorbed ARS on (a) GCE and (b) HPCEE-5H in N_2-saturated 1.0 mol L^{-1} H_2SO_4. Dependence of peak current densities on the scan rate of the ARS low (c, d) and (e, f) high potential redox peaks on (c, e) GCE and (d, f) HPCEE-5H.

Figure S8 show the variations in the anodic and cathodic peak overpotential (E-$E^{0'}$) as a function of log(v) for HPCEE-5H and GCE and electrodes, respectively. By Butler-Volmer theory, the oxidation and reduction rate constants values (k_{ox} and k_{red}, respectively) were obtained based on the exponential dependence of the rate constants on the overpotential using equations 1 and 2.

$$k_{red} = k^0 \, exp\left(\frac{-\alpha nF(E-E^{0'})}{RT}\right) \quad (1)$$

$$k_{ox} = k^0 \, exp\left(\frac{(1-\alpha)nF(E-E^{0'})}{RT}\right) \quad (2)$$

where k^0 is the standard rate constant (at zero overpotential), R is the universal gas constant, F is the faraday constant, T is the temperature, n is the number of electrons transferred, and α is the transfer coefficient representing the degree of symmetry of the energy barrier of the redox reaction.

The value of α can be experimentally estimated from the slope of the straight lines of peak potentials (E_{pa} and E_{pc}) versus log(v) by Laviron method according to equations 3 and 4.[2,15] As the value of α is obtained, k^0 can be calculated by equation 5, where v_a and v_c are the x-intercepts of the anodic and cathodic curves, respectively.

$$slope\left(E_{pa}\, vs.loglog\, v\right) = \frac{2.3\, RT}{(1-\alpha)nF} \quad (3)$$

$$slope\left(E_{pc}\, vs.loglog\, v\right) = \frac{-2.3\, RT}{\alpha nF} \quad (4)$$

$$k^0 = \frac{\alpha nFv_c}{RT} = \frac{(1-\alpha)nFv_a}{RT} \quad (5)$$

The values of k_{red} and k_{ox} were shown in **Table S1**. The values revealed that the kinetic electron transfer of ARS is much faster on HPCEE-5H compared to GCE.

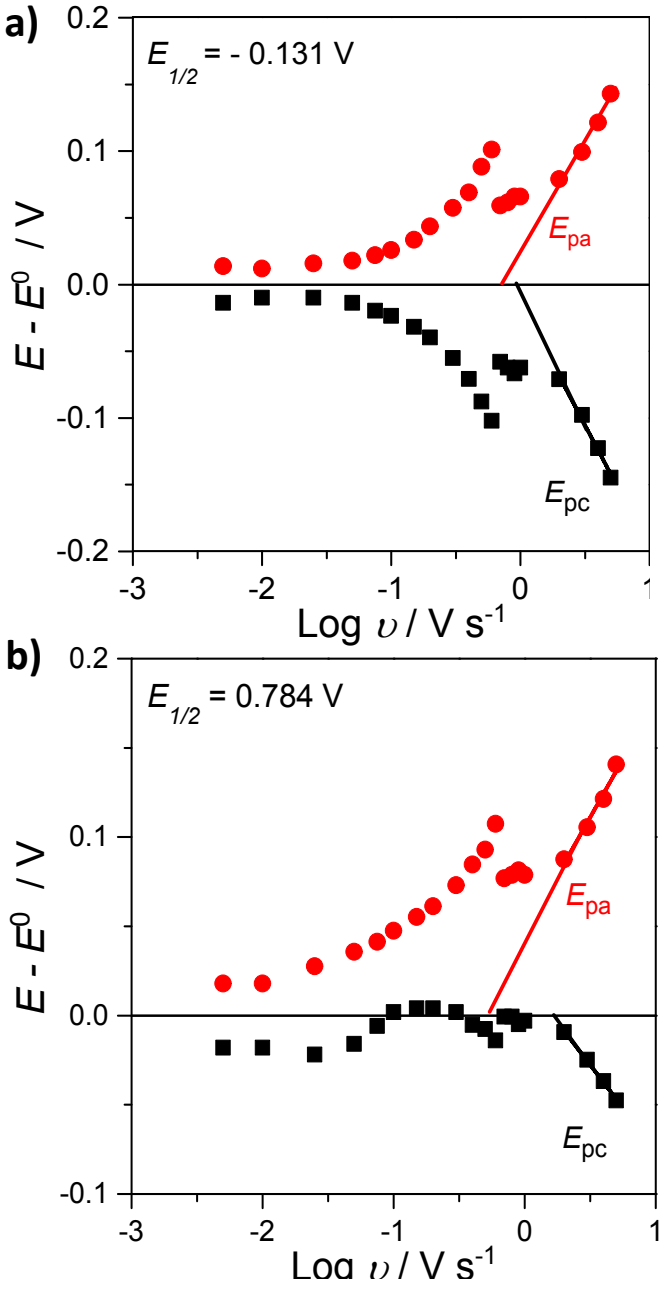

Figure S8. Dependences of the anodic and cathodic overpotentials (E–$E^{0'}$) on the log(v) of the ARS redox peaks at (a) low and b) high potentials on GCE.

Table S1. Values of k_{red} and k_{ox} for the redox process of ARS at low and high potentials on GCE.

Electrode	Low potential		High potential	
	k_{ox} / s^{-1}	k_{red} / s^{-1}	k_{ox} / s^{-1}	k_{red} / s^{-1}
GCE	8.60 ± 4.21	0.79 ± 0.18	21.63 ± 0.50	4.26 ± 3.38
HPCCE-5H	21.22 ± 9.54	16.62 ± 9.37	42.66 ± 11.43	14.23 ± 6.91

S5. Voltammetric profile of the electrodes in the support electrolyte

For comparison, cyclic voltammograms in clean 1.0 mol L^{-1} H_2SO_4 (without ARS) are shown in **Figure S9 and S10**. HEDGE and HPCCE-5H show a redox couple at 0.41 and 0.35 V, respectively, in accordance with the presence of quinone functional groups on carbon-based electrodes (**Figure S9b-d**).[13] Interestingly, this redox couple is not present in GCE (**Figure S9a**) and pristine HPCCE-5H (**Figure S10**), corroborating that these electrodes do not display quinone functional groups on their surfaces.

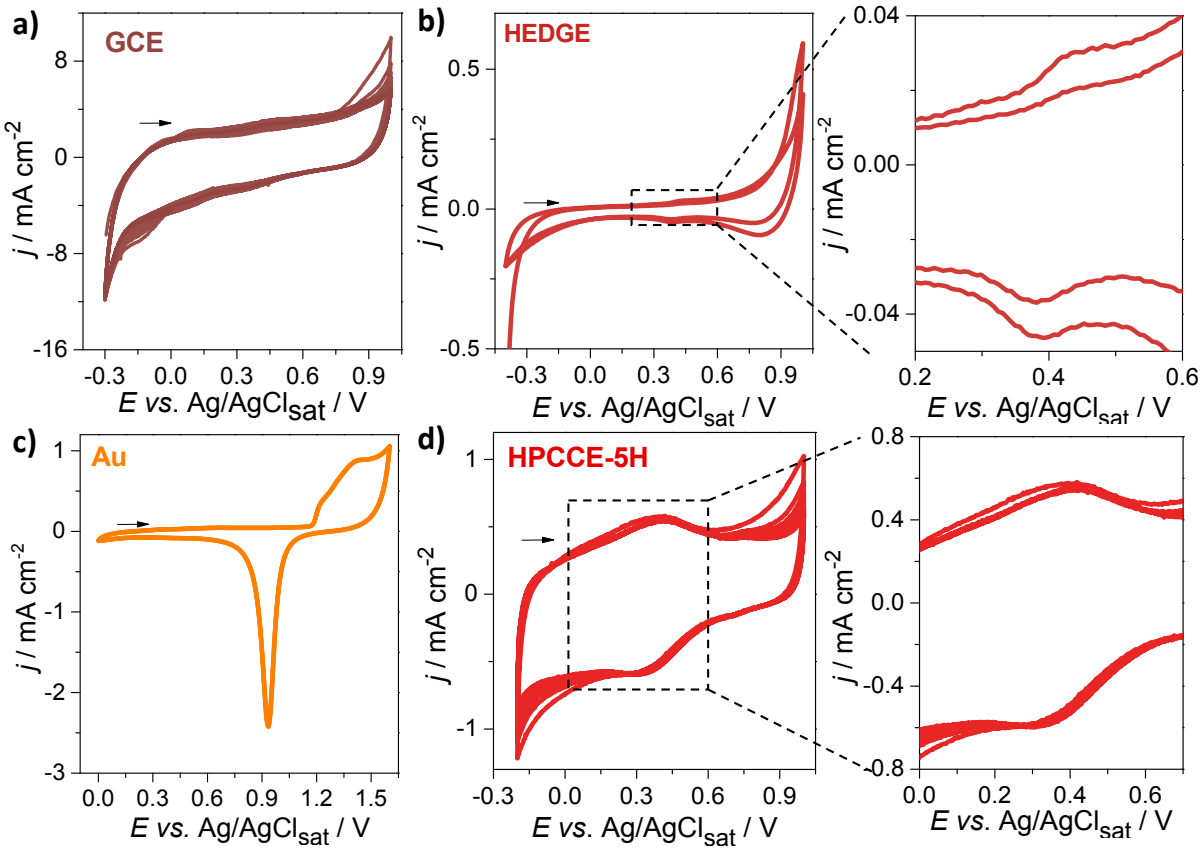

Figure S9. Cyclic voltammograms at 5 mV s^{-1} obtained with (a) GCE, (b) HEDGE, (c) Au disk, and (d) HPCCE-5H in N_2-saturated 1.0 mol L^{-1} H_2SO_4.

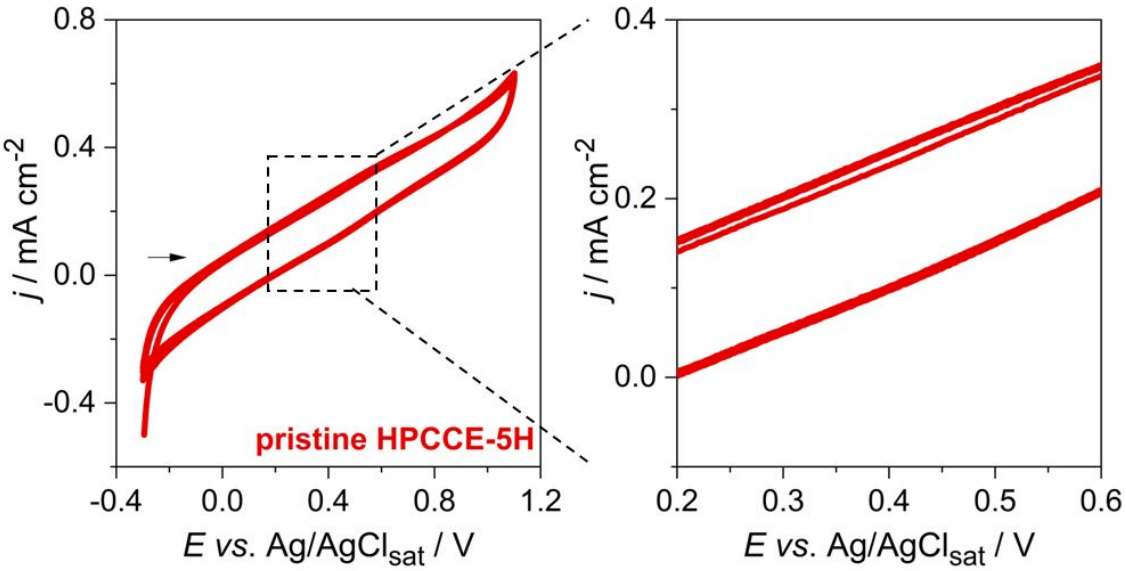

Figure S10. Cyclic voltammogram at 5 mV s^{-1} obtained with pristine HPCCE-5H in N_2-saturated 1.0 mol L^{-1} H_2SO_4.

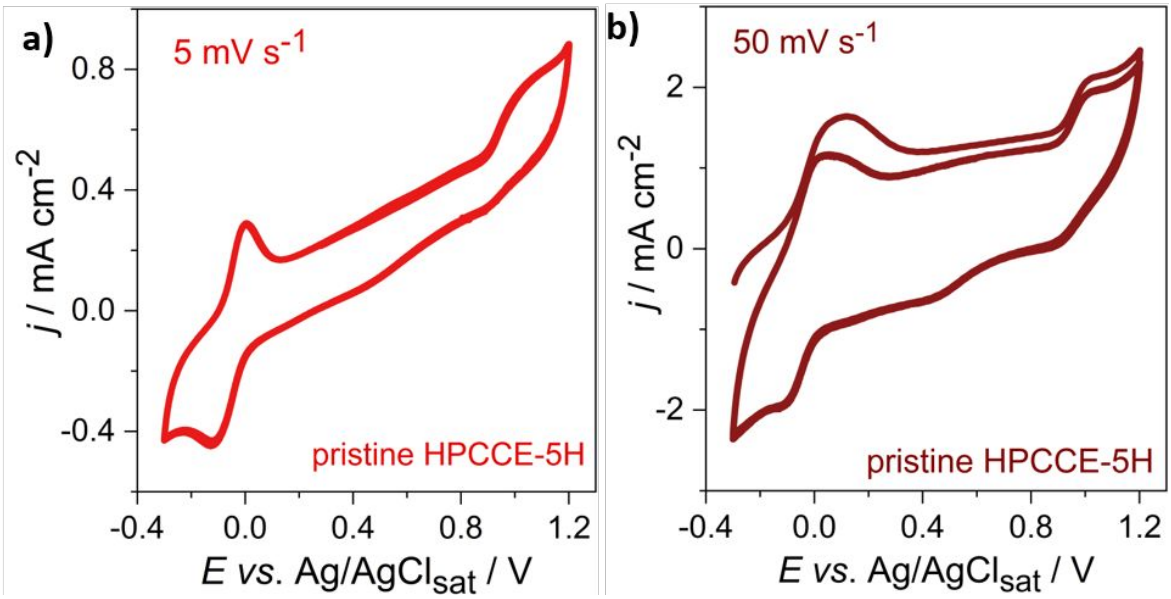

Figure S11. Cyclic voltammograms at (a) 5 mV s^{-1} and (b) 50 mV s^{-1} recorded with pristine HPCCE-5H in 1.0 mol L^{-1} H_2SO_4 containing 1.0 mmol L^{-1} ARS.

S6. Theoretical vibrational and electronic spectra

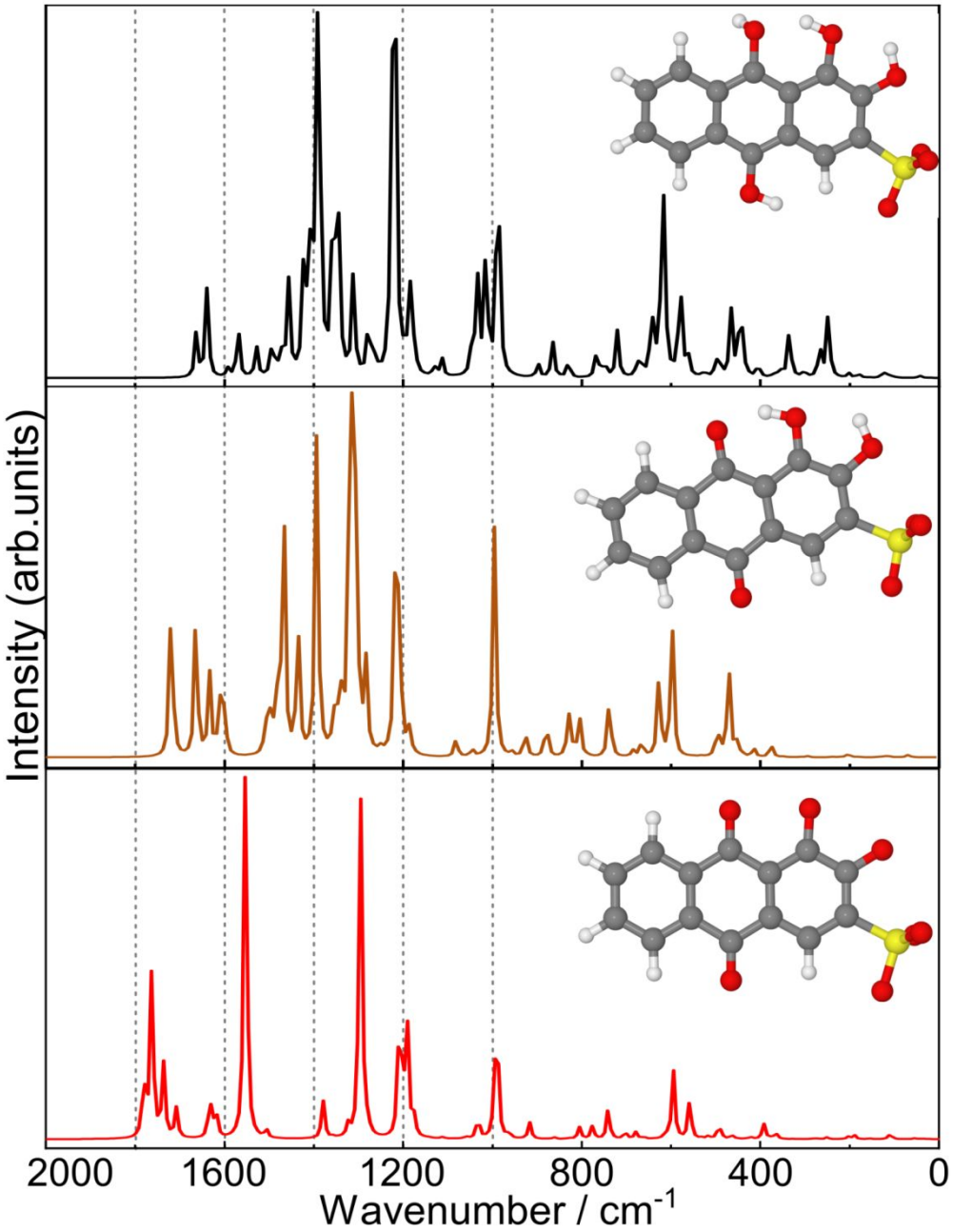

Figure S12. DFT calculated infrared spectra for reduced (upper, black), intermediate (middle, yellow) and oxidized (bottom, red) forms. Dashed lines every 200 cm^{-1} and the molecules at each state were added to ease visualization. Carbon is represented in grey, hydrogen in white, oxygen in red and sulfur in yellow. Artificial broadening was employed to generate the infrared bands. No negative modes were obtained.

S7. Experimental vibrational spectra

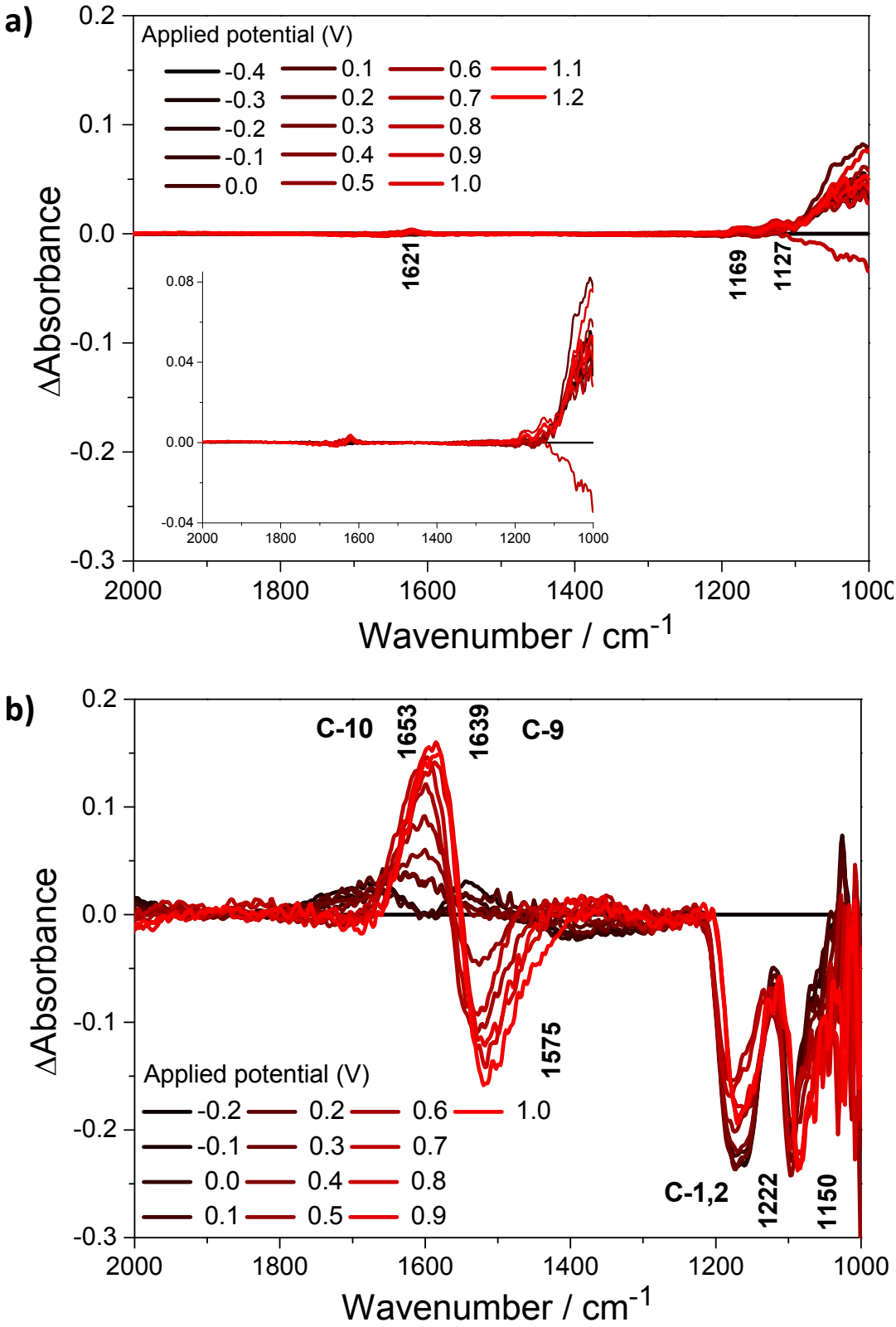

Figure S13. In-situ FTIR spectra in 1.0 mol L^{-1} H_2SO_4 in (a) absence and (b) presence of 1.0 mmol L^{-1} ARS collected at increasing potentials from -0.4 V to + 1.2 V, bare gold electrode.

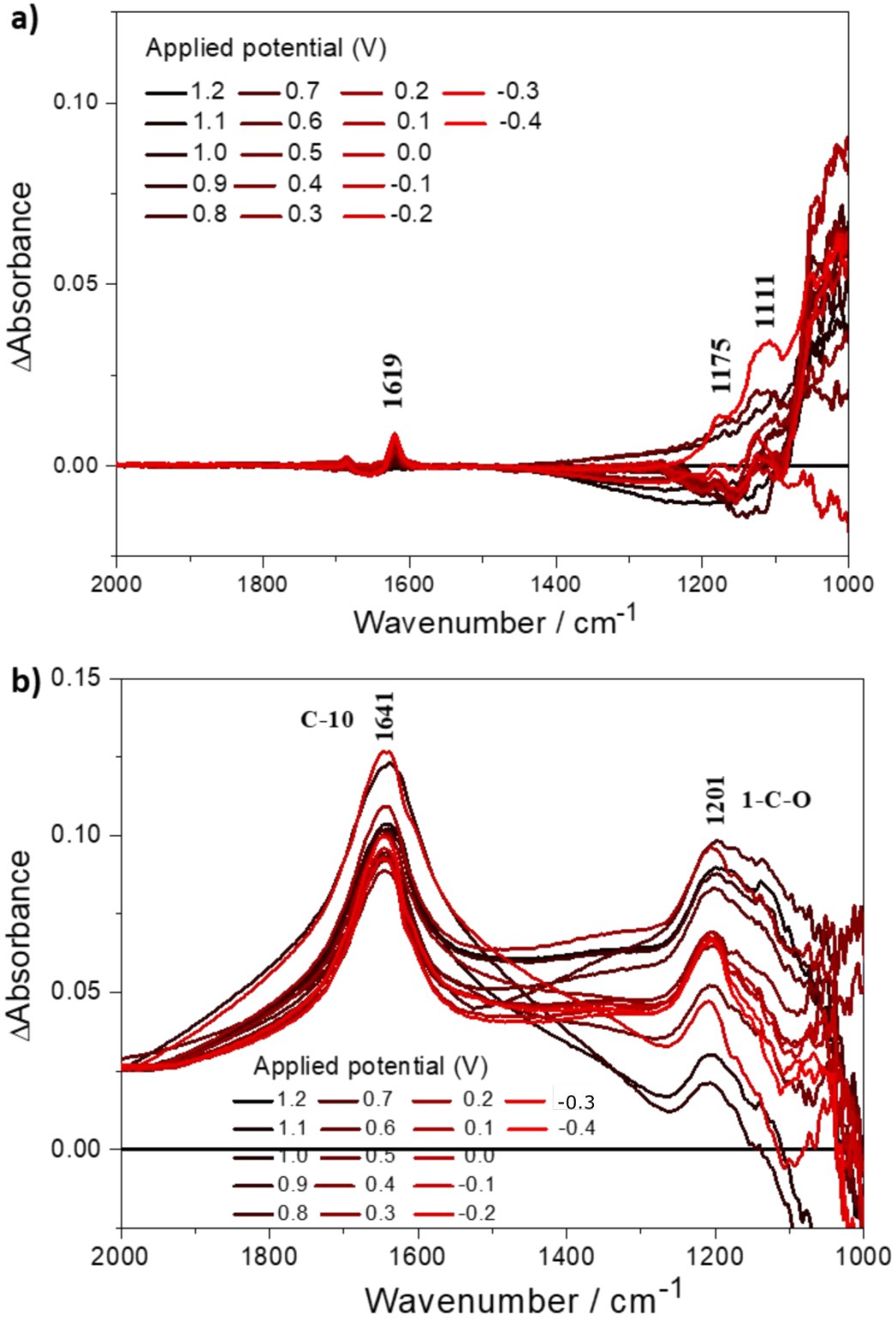

Figure S14. In-situ FTIR spectra in 1.0 mol L^{-1} H_2SO_4 in (a) absence and (b) presence of 1.0 mmol L^{-1} ARS collected at decreasing potentials from +1.2 V to -0.4 V, bare gold electrode.

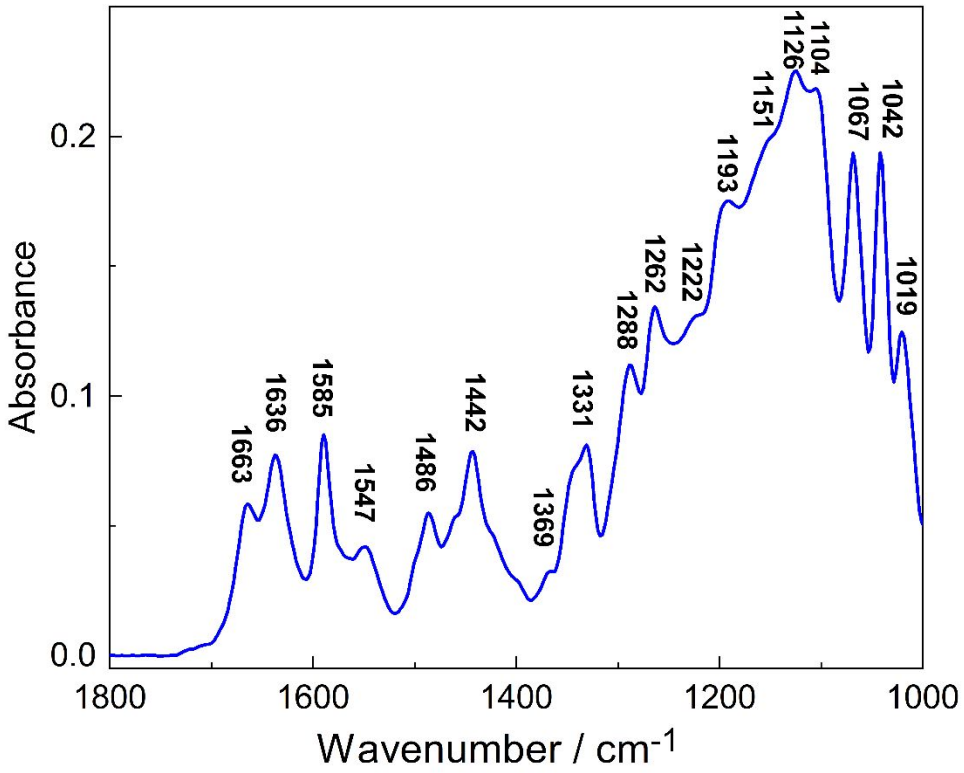

Figure S15. FTIR spectrum of solid ARS on ATR mode.

Table S2. Assignment of the main ARS vibrational modes.[16]

Assignment	**Wavenumber / cm^{-1}**
υ 10-(C=O)	1748
υ 9-(C=O)	1634
υ 9-(C=O)	1634
$\upsilon\ (C=C)_{arom}$	1589
$\upsilon\ (C=C)_{arom}$	1557
υ (C=O)/υ (CC)/δ (C-H)	1503
δ (C-OH)/υ (C-C)/δ (C-H)	1460
$\upsilon\ (C=C)_{arom}$	1447
δ (C-OH)/υ (C-C)	1399/1376
υ (C-C)	1329
υ 2-(C—O)	1292
υ 1-(C—O)	1266
υ C=O/δ (C-C-C)	1202
$\upsilon_{AS}(SO_3)$	1100
$\upsilon_{S}(SO_3)$	1067
δ (C-C-C)/υ (C-C)/ δ (C-H)	1040
υ (C-C)/δ (C-C-C)	1020

S8. In situ electronic spectroscopy

UV–vis absorption spectra were recorded using a Jasco V-670 spectrophotometer in the range 800-200 nm, with a quartz cuvette (1.0 cm pathlength). Different electrochemical potentials ranging from –0.20 V to 1.20 V (vs. $Ag/AgCl_{sat}$) were applied on HPCCE-5H working electrode in 1.0 mol L^{-1} H_2SO_4 containing 0.1 mmol L^{-1} ARS and electronic spectra were recorded when steady-state currents were achieved. The measurements were performed in triplicate at room temperature and N_2 atmosphere.

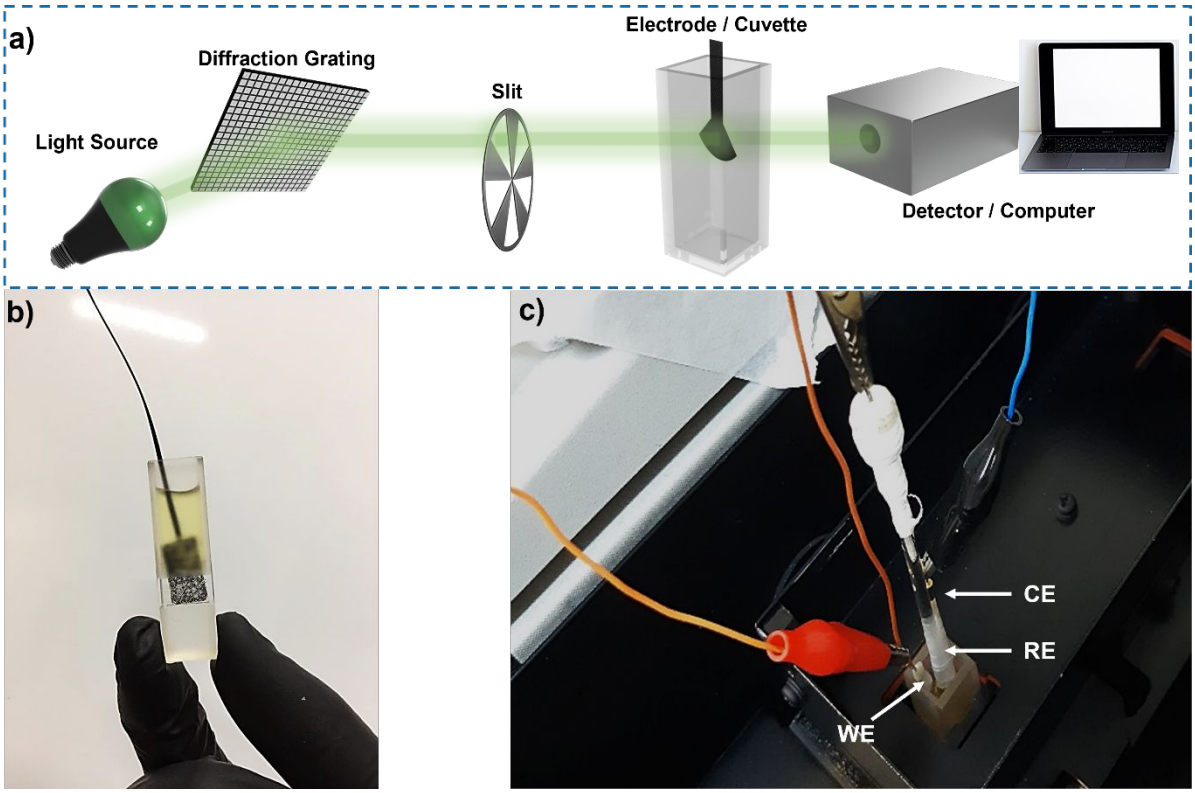

Figure S16. (a) In situ electronic spectroscopic setup schematic, (b) quartz cuvette as the electrochemical cell with ARS solution and the working electrode, and (c) electrochemical cell with the working (WE), reference (RE), and counter electrodes (CE).

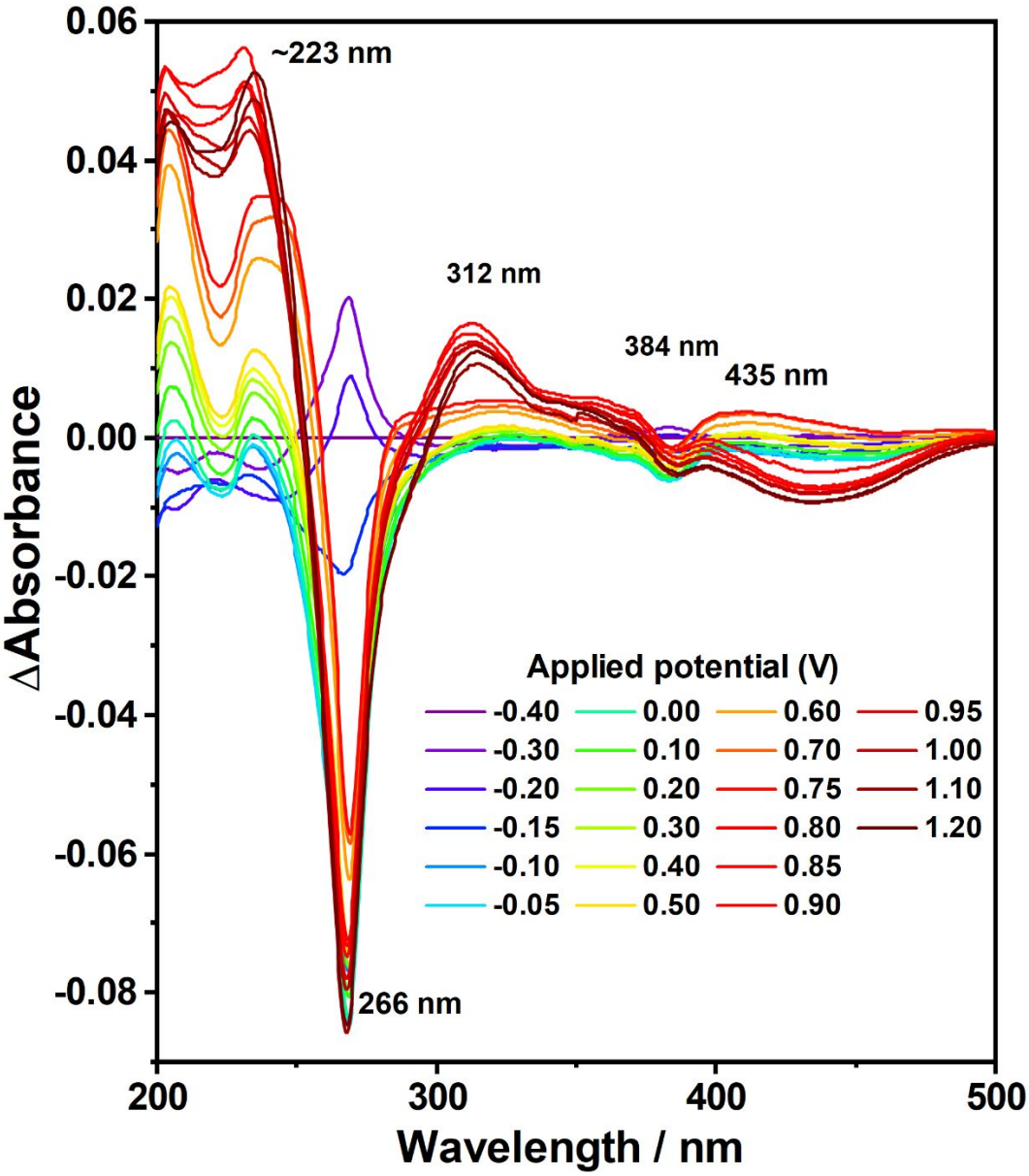

Figure S17. In-situ electronic spectroscopy for ARS oxidation. This is the same data from Figure 2g, enlarged and with a more contrasting colour scheme to aid visualization.

S9. Experimental and Calculated electronic spectra

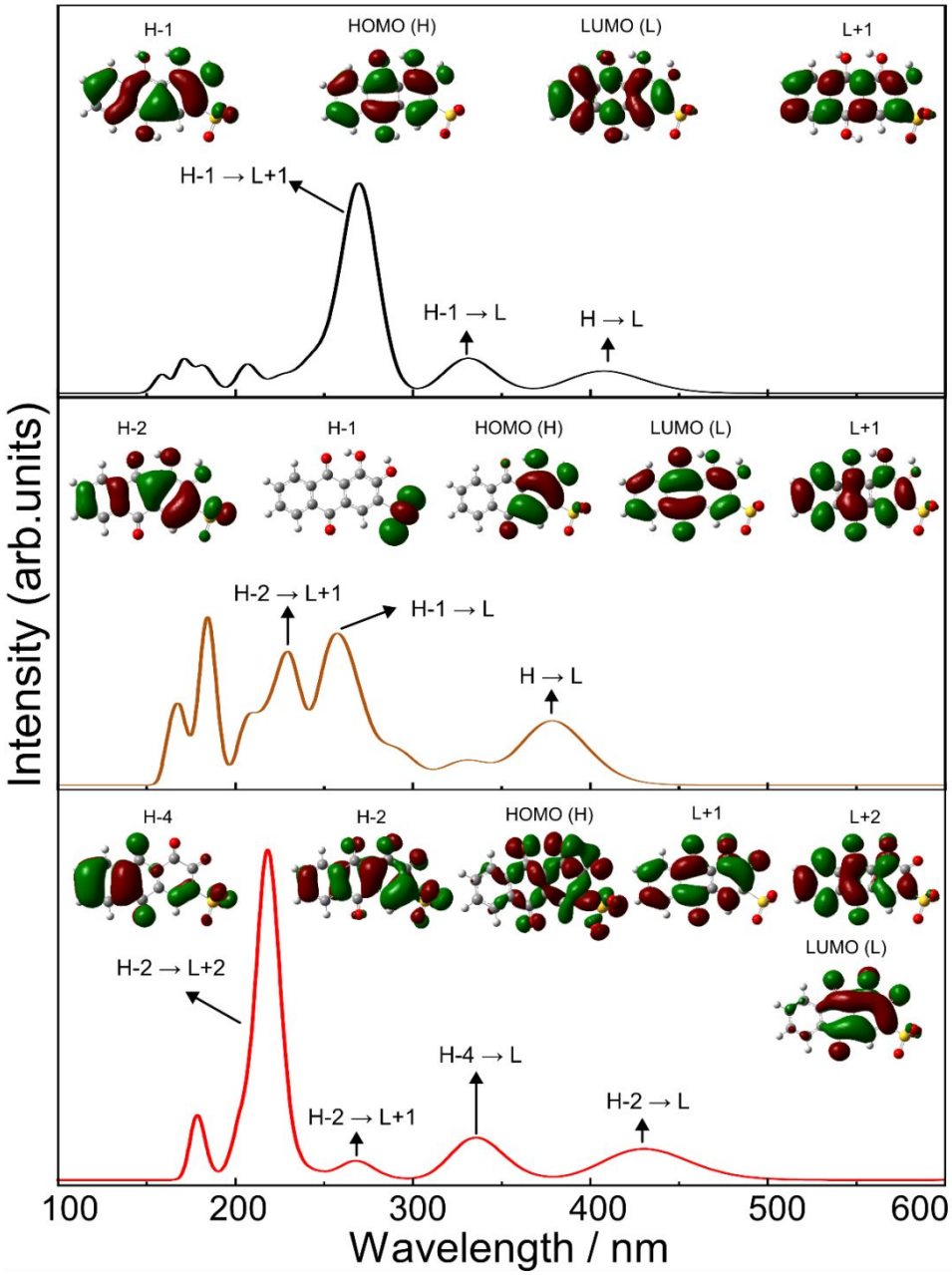

Figure S18. DFT calculated UV-vis spectra for reduced (upper, black), intermediate (middle, yellow) and oxidized (bottom, red) forms, with estimated transitions. Insets: TDDFT-generated molecular orbitals for the reduced (upper), intermediate (middle) and oxidized (bottom) states of the ARS. Color scheme is employed as previously described. Artificial broadening was used to generate the bands. A 40-transition window was selected for TD-DFT for each state.

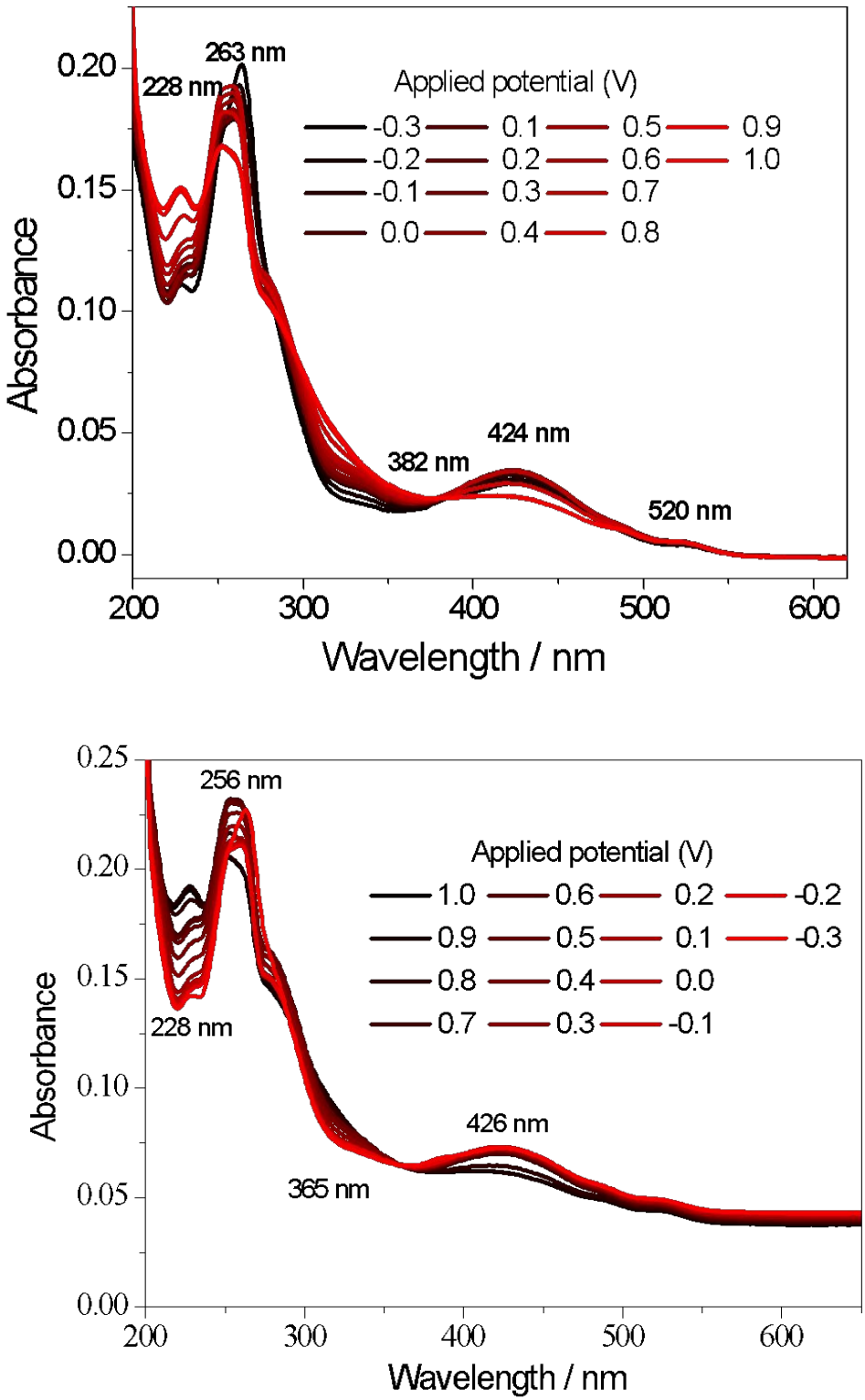

Figure S19. In-situ UV-vis spectra recorded with HPCCE-5H in 1.0 mol L^{-1} H_2SO_4 containing 1.0 mmol L^{-1} ARS, collected varying the applied potential from (a) -0.3 V to +1.2 V and (b) from +1.0 V to -0.3 V.

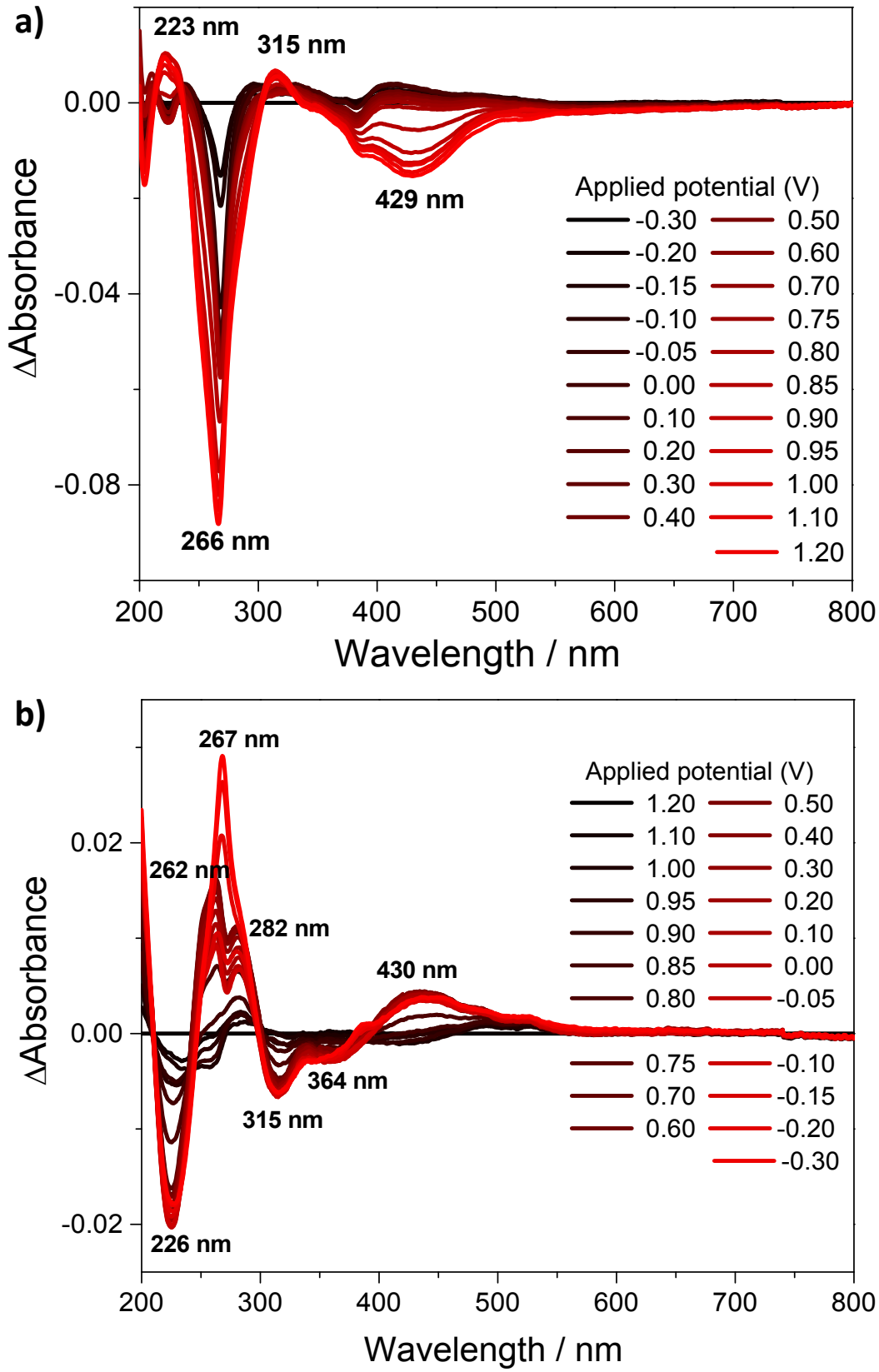

Figure S20. Differential in-situ UV-vis spectra recorded with HPCCE-5H in 1.0 mol L^{-1} H_2SO_4 containing 1.0 m mol L^{-1} ARS, collected varying the applied potential from (a) -0.3 V to +1.2 V and (b) from +1.2 V to -0.3 V.

Table S3. Assignment of the main ARS bands and isosbestic point in the UV-vis spectra.[17,18]

Wavelength / nm	Assignment
226-228	π-π* in benzenoid groups
256-267	π-π* in quinonoid groups
364	isosbestic point, n-σ* intramolecular electron transfer
424-430	n-π * in partially ionized hydroxyl groups

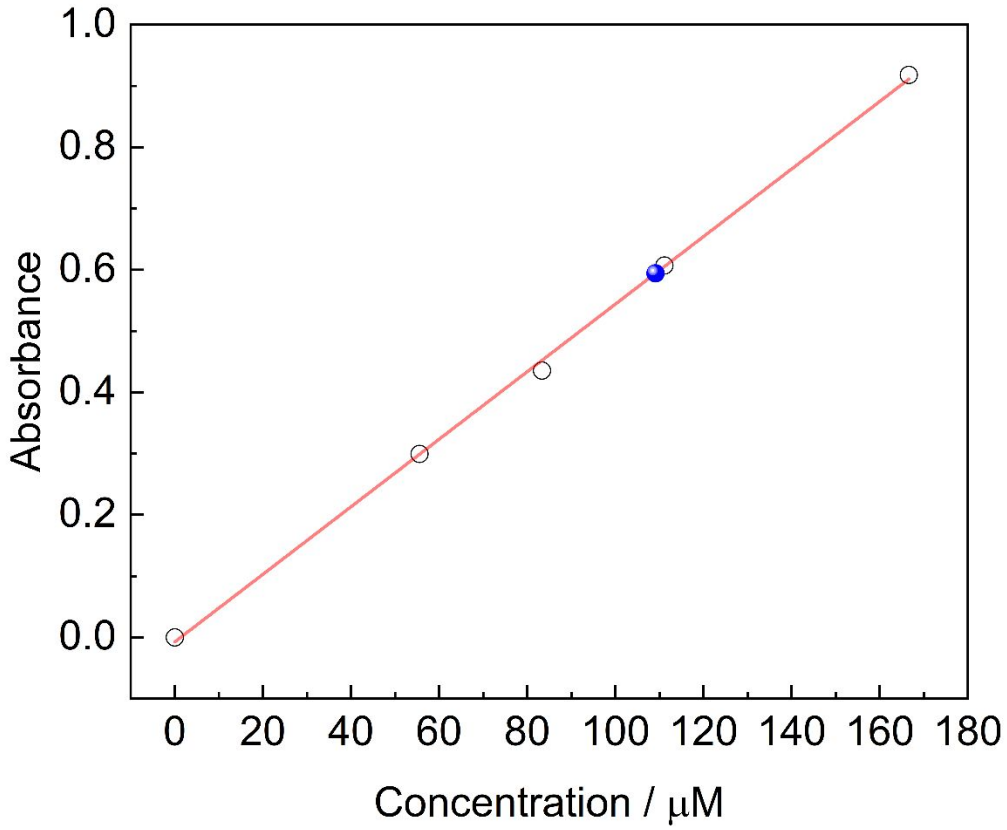

Figure S21. ARS 24h-crossover measurement through electronic spectroscopy. One compartment consisted of ARS 10 mmol L^{-1} in 1.0 mol L^{-1} H_2SO_4 and the other consisted of 1.0 mol L^{-1} H_2SO_4 without ARS. A flow rate of 14.3 mL min^{-1} was employed, the same used for all RFB data. The undiluted sample from the H_2SO_4 compartment had the absorbance measured (blue circle) and compared to diluted samples of the ARS (open circles). An estimated crossover of 1.09% over a 24h period is calculated.

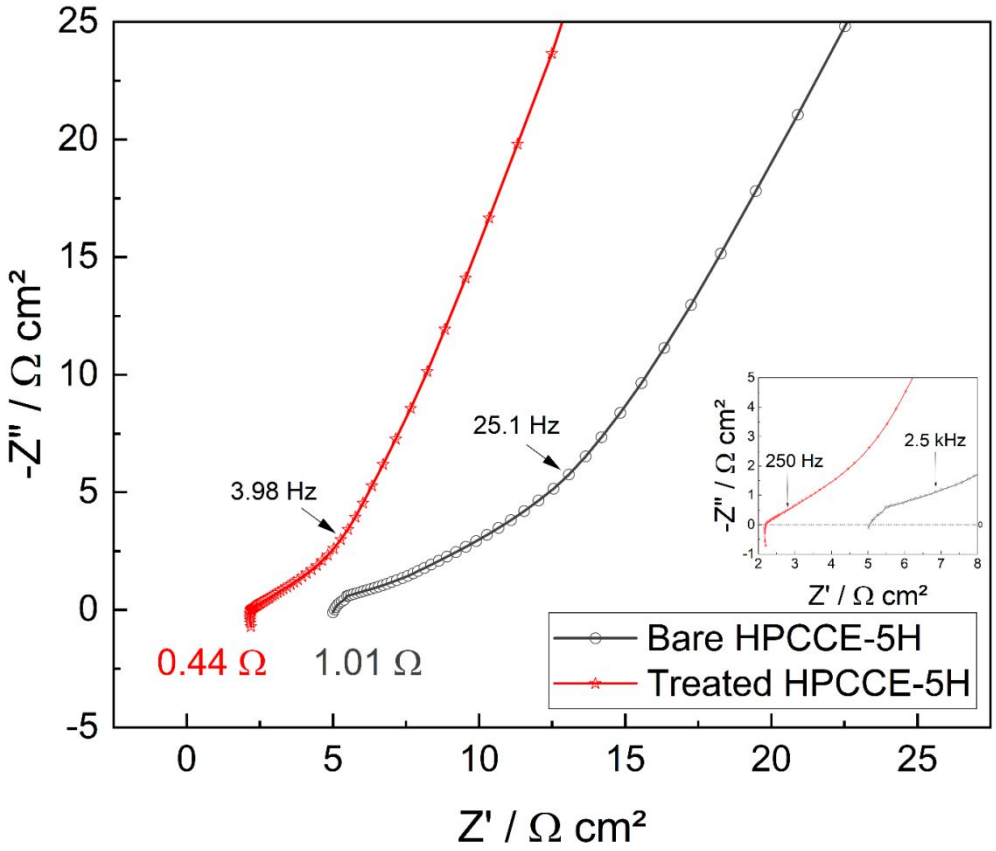

Figure S22. Electrochemical impedance spectroscopy (EIS) comparing the usual chemically treated HPCCE-5H that comprises the stabilization of ARS (red) and the same material without treatments to induce surface stabilization (grey); zoomed-in inset shown to aid visualization.

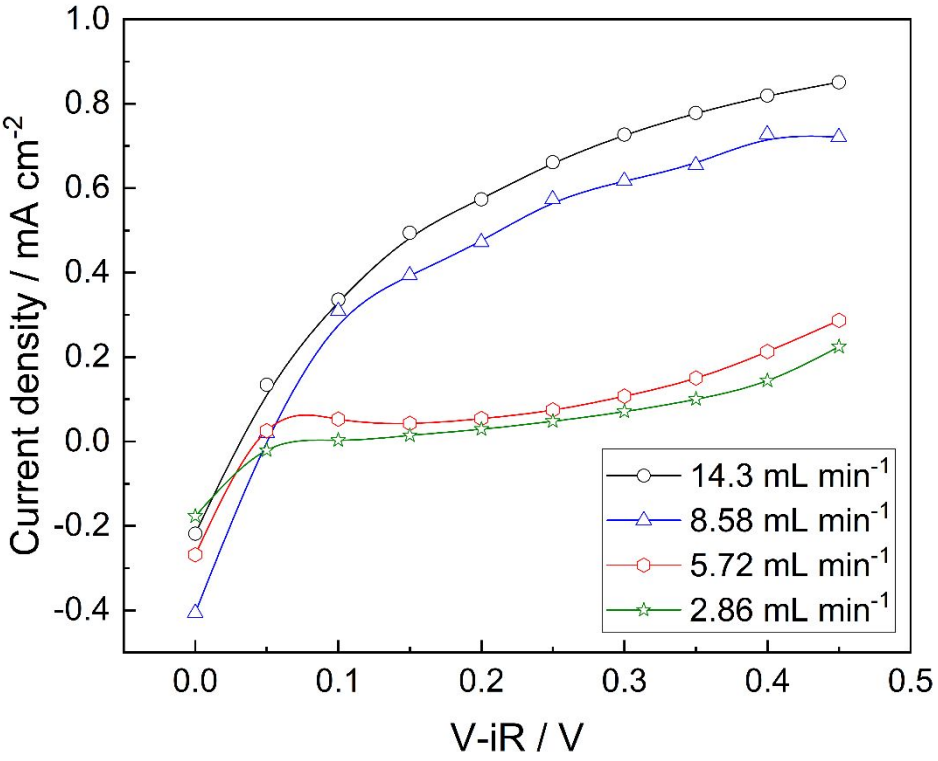

Figure S23. Optimization of the pump flow rate for the RFB using ARS as the redox species in the electrolyte and HPCCE-5H as the electrode material. Data points were obtained by potentiostatic polarization method. The highest pumping rate was selected due to the higher achievable current. All data corrected for iR-drop.

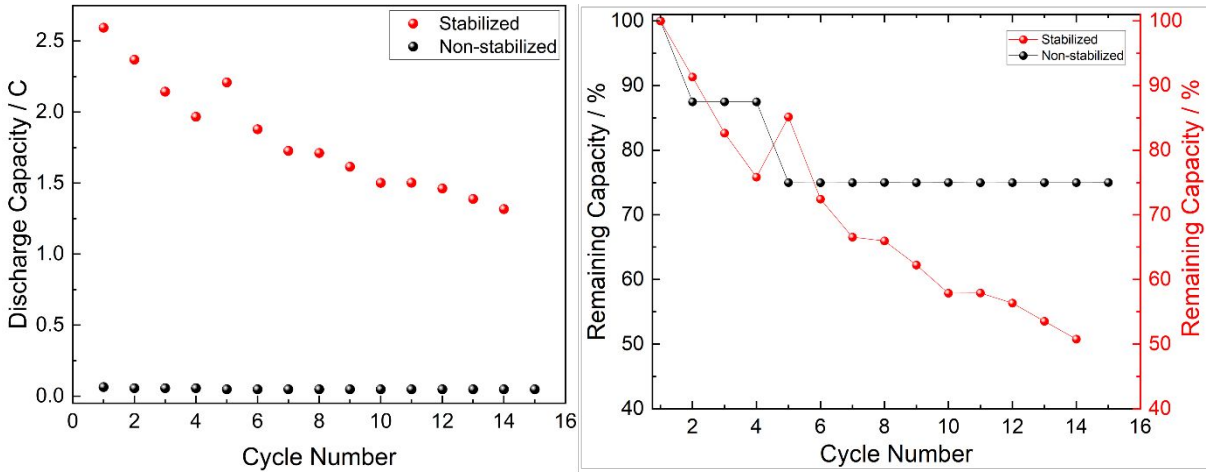

Figure S24. (Left) Discharge capacity fade measured with the HPCCE-5H with ARS stabilization capability (red) and without (black). (Right) Calculated remaining capacities from the same systems, with the larger percentual loss in the untreated HPCCE-5H (black).

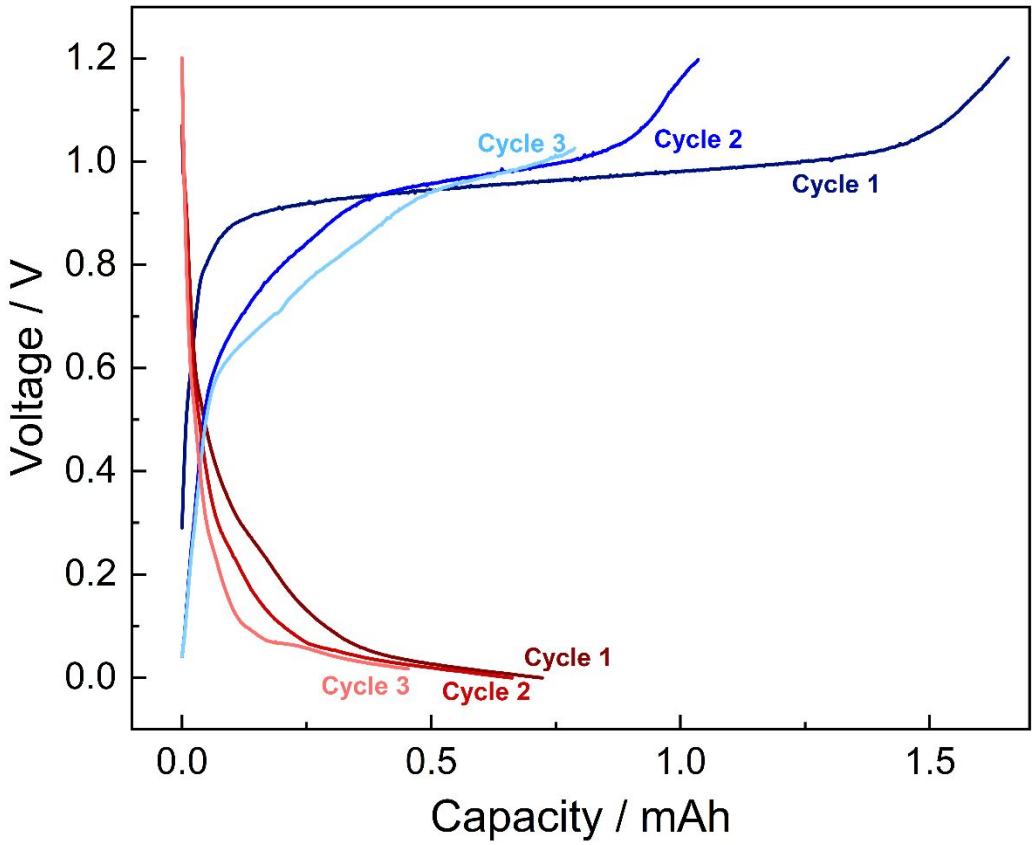

Figure S25. Voltage-Capacity curves for the first three cycles of charge and discharge, as indicated by the colours.

REFERENCES

(1) Sedenho, G. C.; De Porcellinis, D.; Jing, Y.; Kerr, E.; Mejia-Mendoza, L. M.; Vazquez-Mayagoitia, Á.; Aspuru-Guzik, A.; Gordon, R. G.; Crespilho, F. N.; Aziz, M. J. Effect of Molecular Structure of Quinones and Carbon Electrode Surfaces on the Interfacial Electron Transfer Process. *ACS Appl. Energy Mater.* **2020**, *3* (2), 1933–1943. https://doi.org/10.1021/acsaem.9b02357.

(2) Martins, M. V. A.; Pereira, A. R.; Luz, R. A. S.; Iost, R. M.; Crespilho, F. N. Evidence of Short-Range Electron Transfer of a Redox Enzyme on Graphene Oxide Electrodes. *Phys. Chem. Chem. Phys.* **2014**, *16* (33), 17426–17436. https://doi.org/10.1039/C4CP00452C.

(3) Kohn, W.; Sham, L. J. Self-Consistent Equations Including Exchange and Correlation Effects. *Phys. Rev.* **1965**, *140* (4A), A1133–A1138. https://doi.org/10.1103/PhysRev.140.A1133.

(4) Hohenberg, P.; Kohn, W. Inhomogeneous Electron Gas. *Phys. Rev.* **1964**, *136* (3B), B864–B871. https://doi.org/10.1103/PhysRev.136.B864.

(5) M. J. Frisch, G. W. Trucks, H. B. Schlegel, G. E. Scuseria, M. A. Robb, J. R. Cheeseman, G. Scalmani, V. Barone, G. A. Petersson, H. Nakatsuji, X. Li, M. Caricato, A. Marenich, J. Bloino, B. G. Janesko, R. Gomperts, B. Mennucci, H. P. Hratchian, J. V. Ort, and D. J. F. Gaussian. 2016.

(6) Neese, F. The ORCA Program System. *WIREs Comput. Mol. Sci.* **2012**, *2* (1), 73–78. https://doi.org/10.1002/wcms.81.

(7) Becke, A. D. Density-Functional Thermochemistry. III. The Role of Exact Exchange. *J.*

Chem. Phys. **1993**, *98* (7), 5648–5652. https://doi.org/10.1063/1.464913.

(8) Ullrich, C. A.; Yang, Z. A Brief Compendium of Time-Dependent Density Functional Theory. *Brazilian J. Phys.* **2014**, *44* (1), 154–188. https://doi.org/10.1007/s13538-013-0141-2.

(9) Suarez, E. D.; Lima, F. C. D. A.; Dias, P. M.; Constantino, V. R. L.; Petrilli, H. M. Theoretical UV-Vis Spectra of Tetracationic Porphyrin: Effects of Environment on Electronic Spectral Properties. *J. Mol. Model.* **2019**, *25* (9), 264. https://doi.org/10.1007/s00894-019-4149-6.

(10) Wolinski, K.; Hinton, J. F.; Pulay, P. Efficient Implementation of the Gauge-Independent Atomic Orbital Method for NMR Chemical Shift Calculations. *J. Am. Chem. Soc.* **1990**, *112* (23), 8251–8260. https://doi.org/10.1021/ja00179a005.

(11) Adamo, C.; Barone, V. Toward Reliable Density Functional Methods without Adjustable Parameters: The PBE0 Model. *J. Chem. Phys.* **1999**, *110* (13), 6158–6170. https://doi.org/10.1063/1.478522.

(12) Faria, L. C. I.; Sedenho, G. C.; Bertaglia, T.; Macedo, L. J. A.; Crespilho, F. N. A Comparative Study of Chemically Oxidized Carbon Cloth and Thermally Treated Carbon Paper Electrodes Applied on Aqueous Organic Redox Flow Batteries. *Electrochim. Acta* **2024**, *485*, 144086. https://doi.org/10.1016/j.electacta.2024.144086.

(13) Ali, M. A.; Hassan, A.; Sedenho, G. C.; Gonçalves, R. V.; Cardoso, D. R.; Crespilho, F. N. Operando Electron Paramagnetic Resonance for Elucidating the Electron Transfer Mechanism of Coenzymes. *J. Phys. Chem. C* **2019**, *123* (26), 16058–16064. https://doi.org/10.1021/acs.jpcc.9b01160.

(14) Ali, M. A.; Sedenho, G. C.; Pacheco, J. C.; Iost, R. M.; Rahman, A.; Hassan, A.; Cardoso, D. R.; Gomes, R. S.; Crespilho, F. N. Metal-Free, Low-Cost, and High-Performance Membraneless Ethanol Fuel Cell. *J. Power Sources* **2022**, *551*, 232164. https://doi.org/10.1016/j.jpowsour.2022.232164.

(15) Luz, R. A. S.; Pereira, A. R.; de Souza, J. C. P.; Sales, F. C. P. F.; Crespilho, F. N. Enzyme Biofuel Cells: Thermodynamics, Kinetics and Challenges in Applicability. *ChemElectroChem* **2014**, *1* (11), 1751–1777. https://doi.org/10.1002/celc.201402141.

(16) Legan, L.; Retko, K.; Ropret, P. Vibrational Spectroscopic Study on Degradation of Alizarin Carmine. *Microchem. J.* **2016**, *127*, 36–45. https://doi.org/10.1016/j.microc.2016.02.002.

(17) Olivier Thomas, C. B. *UV-Visible Spectrophotometry of Water and Wastewater*; Elsevier, 2017.

(18) Peters, R. H.; Sumner, H. H. 430. Spectra of Anthraquinone Derivatives. *J. Chem. Soc.* **1953**, 2101. https://doi.org/10.1039/jr9530002101.